A Laser System for Cooling and Trapping Potassium-39

Marcel Duda

Munich 2017

Ein Laseraufbau zum Kühlen und Fangen von Kalium-39

Masterarbeit an der Fakultät für Physik
Ludwig-Maximilians-Universität München
Max-Planck-Institut für Quantenoptik

vorgelegt von

Marcel Duda

München, den 9. November 2017

Contents

CHAPTER 1

Introduction

Before the discovery of lasers, the lowest reachable temperatures for atoms, e.g. liquid helium, were around 4 Kelvin. At these temperatures, the helium atoms have an average speed of about 90 m/s [1]. Measurements on such "hot" samples are difficult due to the broad velocity distributions, not to mention the poor controllability. Based on the first proposals for laser cooling in the 1970s [2, 3], the field developed numerous approaches in the 1980s to get cold and trapped atomic samples. This includes pre-cooling with a Zeeman-slower [4–6], Doppler cooling [7], cooling and trapping in a magneto-optical trap [8] or breaking the recoil limit by velocity selective coherent population trapping [9]. Equipped with sophisticated cooling techniques, it was feasible to observe the "holy grail" of atomic, molecular and optical (AMO) physics, the Bose-Einstein Condensate (BEC). Nearly a decade after its prediction, the BEC was measured at JILA in 1995 [10, 11].

Besides investigations and exploitations of principle properties of the BEC such as observing interferences in BECs [12] or creating an atom laser [13], it was understood that one can now use non-condensed ultracold atoms, for example in optical lattices [14], to investigate phase diagrams of Hubbard models [15] and describe the hopping of atoms in a lattice with on-site interaction. The phase diagrams were mapped out by probing phase transitions, e.g. from the superfluid to the Mott-Insulator [16]. Due to the possibilities to manipulate atoms and sophisticated detection methods, ultracold atoms became a promising and diverse platform for quantum simulation. Additionally, quantum gas microscopy [17] has become a useful tool that allows the imaging of single atoms and to obtain full control over the system.

Most of the experiments were limited to lattice systems where the interactions happened only on-site or through second order processes with nearest neighboring sites [18]. With growing interest towards lattice systems with long-range interactions and extensions of the Hubbard models, ways had to be found to create interactions across several sites. One of the possibilities is using magnetic dipolar atoms such as Erbium, Dysprosium and Chromium [19–22]. Other proposals include dipolar molecules [23] and Rydberg atoms [24]. Due to the long-ranged interactions that are controllable in strength and direction, Rydberg atoms have become a prominent candidate. Proposals to discover new phases of matter [25] or to probe extensions to Hubbard Hamiltonians [26, 27] led to realizations of quantum gas microscopes with Rydberg atoms [28, 29].

This Master's thesis examines the progress of constructing a new experimental setup to study quantum many body physics with Rydberg atoms. The focus will be on the design and build-up of a laser system to provide a cooled and trapped sample of Potassium-39. It is divided into five chapters. Having introduced the achievements within the ultracold atom community, starting from laser cooling towards quantum simulation with long-ranged interactions, in the current chapter, Chapter 2 discusses how long range interactions can be achieved with Rydberg atoms, introduces the proposals that we want to realize in our setup and convey the adaptability of our experimental apparatus. Chapter 3 gives a semi-classical derivation of light forces and discusses specific cooling techniques implemented in our laser cooling setup, building the basis for Chapter 4, where the experimental apparatus is presented. Starting from the properties of Potassium-39, a full-scale description and characterization of the laser system, a summary of the vacuum system and a discussion of the cooling sequence is given. Finally, Chapter 5 concludes this thesis by summarizing the status of the experimental construction and by providing an outlook for the future steps towards a quantum simulator with Rydberg atoms.

CHAPTER 2

Quantum Many-Body Physics with Rydberg Atoms

The goal of our setup is to create a versatile experimental platform with potassium for the study of quantum many-body phenomena [30], quantum simulation [31], interaction driven topological phases [32] and investigations of other fundamental questions of quantum physics such as non-equilibrium dynamics [33].

The many applications that we want to realize in our system come from the flexibilities provided by Rydberg atoms. Rydberg atoms have an electron in a high-lying electronic state leading to exaggerated properties [24]. The interaction strength of Rydberg atoms is comparable to ions and about 12 orders of magnitude higher than ground state atoms [34]. In contrast to ions, the interaction strength can quickly be switched on and off which is useful for the implementation of quantum gates [35]. In addition to the interaction strength, the interactions can be tuned to be attractive or repulsive and isotropic or anisotropic. The implementation of Rydberg atoms into quantum simulators or for quantum information limits the time-scale of the experiment. The timescales of tens of microseconds, due to radiative or black-body induced decay, are too short to probe motional dynamics. Even though the lifetime increases for higher principle quantum numbers, the system will remain within the frozen gas regime [36] throughout the experiment. A way to increase the lifetimes of Rydberg atoms is to perform the experiments within a cryogenic environment [37]. Realizing a cryogenic environment for an ultracold experiment is very challenging due technical difficulties. An alternative is to increase the experimental lifetime through the use of the so-called Rydberg dressing [38]. Rydberg dressing describes the admixing of a small fraction of the Rydberg state character to a ground state atom. Therefore, the Rydberg character is less exaggerated leading to weaker interactions, but still orders of magnitude higher than ground state atoms. On the other hand, the lifetime of the dressed atoms can be increased by orders of magnitude compared to the bare Rydberg atom [39, 40]. The small admixture results from the level-shifts due the interacting atoms. For small distances, characterized by the Rydberg blockade [41], the interaction strength will shift the doubly excited Rydberg state so far out of resonance that only one Rydberg atom can be excited.

For our experimental platform to remain as simple and as powerful as possible, we planned to implement several approaches for a quantum simulator. Two excitation schemes will allow for the excitation of Rydberg atoms or Rydberg dressed

atoms. Detection through an ion detector enables us to probe Rydberg atoms while quantum gas microscopy with a high-NA objective gives us a sophisticated detection method. We are going to attempt to employ two loading schemes, the optical lattices and microtraps giving us the option to probe systems in very different regimes.

The two Rydberg excitation schemes will gives us the possibility to engineer intrinsically different interactions. With the one-photon excitation scheme, consisting of two doubling stages generating UV-light, we can transfer atoms from $4S \rightarrow nP$. The tunability for the laser system allows us to excite to all states starting from 20P to ionization. With the valence electron in the p-state, the interactions can be anisotropic and its strength can be changed with the laser detuning. We can therefore tune the interaction strength depending on the Rydberg state that we are coupling to. The longer lifetimes and tunable interaction strengths enable us to move outside the frozen gas regime and study motional dynamics. With the two-photon excitation scheme [42], we can excite Rydberg atoms. Two lasers, one for the $4S \rightarrow 5P$ transition at 405 nm and the $5P \rightarrow nS/nD$ transition at 970 nm will be needed for this approach. Comparing the Rabi frequencies in the case of Rubidium in [43], we know that a Rydberg dressing scheme will not be possible with the two-photon transition. Instead, we can use the two-photon scheme to address the isotropic nS-states, leading to isotropic interactions, or possibly the nD-states for more exotic interaction profiles. With a high-NA objective, we can do single-site addressing of the Rydberg atoms with the 970 nm light.

The detection of the Rydberg atoms will be performed through a quantum gas microscope [17, 44, 45] with the use of the aforementioned high-NA objective. For destructive measurements, we can use an ion detector where presence of Rydberg atoms can be quickly probed while the actual position will remain unknown. However, the quantum gas microscope will allow for full detection and control of the system. From the microscopic images, we will be able to extract the position of the atoms, observe the dynamics through consecutive shots which allows us to measure correlation functions [46].

The two trapping schemes that we are trying to employ in our setup are optical lattices and microtraps. Optical lattices have become a standard technique for ultracold atoms experiments. Counter-propagating laser beams create a periodic potential where the atoms get trapped at the positions of highest or lowest intensity [47]. Depending on the beam parameters, one can tune the coupling strength between the lattice sites relative to the on-site interaction which led to the observation of a superfluid to Mott Insulator transition [16]. For optical lattices, the tunneling strength and the on-site interaction are comparable. In the case of microtraps, referring to optical dipole traps, the tunneling strength is suppressed and the dynamics of the system are related to interaction dominated internal degrees of freedom. The advantage of the microtraps is that they can be loaded after considerably shorter preparation times. Pushing the cooling sequence to its limits, the loading time could be reduced by one or two orders of magnitude. In systems where optical lattices and microtraps are both

feasible, the microtraps will allow us to quickly collect statistics. Fast repetition rates will make it possible for us to measure entanglement entropy which requires to know the full reduced density matrix, the dimensions of which grow exponentially with the system size [48], in our case, the number of atoms in the traps.

There are several experiments that can be realized in our setup. One of the goals is to observe supersolids [49, 50], a novel phase of matter which is a superfluid that breaks translation symmetry. Furthermore, recent interest was sparked in probing topological phases in interacting, driven systems [32, 51]. Given that the proposals rely on interaction dominated dynamics, these phase transitions could be observed in our microtraps setups. Within the field of quantum information, we might attempt to create quantum gates [52] with Rydberg atoms. Finally, quantum simulation will remain one of the most prominent applications of our setup. Quantum magnetic Ising-like systems with long-range interactions have already been successfully realized [28]. With the rich interaction of Rydberg dressed systems, we attempt to realize more exotic Hamiltonians including, but not limited to, studies of quantum spin-ice [53] and frustrated quantum magnets [54].

CHAPTER 3

Cooling and Trapping with Light

This chapter will discuss key concepts of cooling and trapping of neutral atoms with light. To this end, we will derive two different types of light forces on a two-level atom, a conservative and a dissipative force. The treatment shall be brief and conceptual but a more rigorous and elaborate treatment of light forces can be found in [55]. With the light forces in mind, we will be able to understand the working principles of the Zeeman slower, the magneto-optical trap and the grey molasses. These are the cooling and trapping techniques that are implemented in our setup.

3.1 Light Forces

It can be understood from a simple classical picture that there is a light force for an atom in a light field. One can imagine an atom with a dipole moment $\mathbf{d}$, either static or through a non-zero polarizability, in the presence of an electric field $\mathbf{E}$. For such a scenario the potential will be $V = -\mathbf{d} \cdot \mathbf{E}$. Now, if the electric field is not homogeneous in space, as for a focused laser beam, we will have a force from the space-dependent potential. This picture already provides us with intuition for the conservative potential. Unfortunately the details of the electric field and the dipole are not encompassed appropriately and we still did not account for a dissipative force. Therefore, we will resort to a semi-classical derivation of the motion of the center of mass of an atom in the presence of light. We will limit ourselves to the discussion of a two-level system were the size of the atoms is much smaller than the wavelength.

Let us start in the Heisenberg picture where the operators depend on time and the states do not. We want to see the time evolution of the momentum operator $\hat{p}$ given by [56]

$$\frac{d}{dt}\hat{p} = \frac{1}{i\hbar}[\hat{p}, \hat{H}]. \tag{3.1}$$

The left-hand side of equation (3.1) is the force. Note, that the momentum operator has no explicit dependence on time. The Hamiltonian in the commutator is the interaction that couples the ground and the excited state given by

$$\hat{H} = \frac{\hbar}{2}\begin{bmatrix} 0 & \Omega \\ \Omega^* & 0 \end{bmatrix}.$$

We can now represent the momentum operator as $\hat{p} = -i\hbar\nabla$ which gives us

$$\langle \hat{F} \rangle = \mathrm{Tr}(\hat{\rho}\hat{F}) = -\frac{1}{2}\hbar\big(\nabla\Omega\rho_{12} + \nabla\Omega^*\rho_{21}\big). \tag{3.2}$$

Let us note at this point that we can rewrite the average force in terms of the susceptibility $\chi = \frac{\rho_{21}}{\Omega}$ such that the force equals

$$\begin{aligned}\langle \hat{F} \rangle &= \frac{1}{4}\hbar\Omega^*\nabla\Omega\frac{\rho_{12}}{\Omega^*} + \frac{1}{4}\hbar\Omega\nabla\Omega^*\frac{\rho_{21}}{\Omega} \\ &= \underbrace{\hbar\nabla|\Omega|^2 \mathrm{Re}\big(\frac{\rho_{21}}{\Omega}\big)}_{\text{reactive force}} + \underbrace{\frac{1}{2}\hbar|\Omega|^2\nabla\phi\,\mathrm{Im}\big(\frac{\rho_{21}}{\Omega}\big)}_{\text{dissipative force}}.\end{aligned} \tag{3.3}$$

This equation contains two distinct terms. One is a conservative force, also called the reactive force, that we could understand from our previous simple picture. It depends on the gradient of the electric field and on the real part of the susceptibility. The second term on the other hand depends on the imaginary part of the susceptibility and on the change in the phase. It will be clear later that this represents a dissipative force. In order to further investigate the two terms in equation (3.3), we should know the coherence ρ_{21} in terms of the Rabi frequency Ω, the detuning Δ and the linewidth Γ.

Optical Bloch Equations

We can write the time evolution of the density matrix for a two-level atom with a linewidth Γ in the presence of the light field as follows [57]:

$$\dot{\rho}_{11} = \frac{i\Omega}{2}(\rho_{21} - \rho_{12}) + \Gamma\rho_{22} \tag{3.4}$$

$$\dot{\rho}_{22} = \frac{i\Omega}{2}(\rho_{12} - \rho_{21}) - \Gamma\rho_{22} \tag{3.5}$$

$$\dot{\rho}_{12} = \frac{i\Omega}{2}(\rho_{22} - \rho_{11}) - (\frac{\Gamma}{2} + i\Delta)\rho_{21} \tag{3.6}$$

$$\dot{\rho}_{21} = \frac{i\Omega}{2}(\rho_{11} - \rho_{22}) - (\frac{\Gamma}{2} - i\Delta)\rho_{12}. \tag{3.7}$$

The terms that contain the scattering rate have been introduced phenomenologically and result from the fact that the excited state has a certain lifetime associated with it. Treating the two-level system as an open system, implying a coupling to the surroundings, will suffice to get these equations. Looking at these systems in steady-state ($\dot{\rho}_{ij} = 0$), we get

$$\rho_{21} = -i\frac{\Omega}{\Gamma}\frac{1 + \frac{2i\Delta}{\Gamma}}{1 + (\frac{2\Delta}{\Gamma})^2 + 2(\frac{\Omega^2}{\Gamma^2})}, \quad \rho_{22} = \frac{\Omega^2/\Gamma^2}{1 + (\frac{2\Delta}{\Gamma})^2 + 2(\frac{\Omega^2}{\Gamma^2})}. \tag{3.8}$$

Since the light forces are given in terms of $\mathrm{Re}(\rho_{21})$ and $\mathrm{Im}(\rho_{21})$, and by noting that $\rho_{12} = \rho_{21}^*$, we can rewrite the light forces in the following fashion [58]

$$\langle \hat{F} \rangle = \underbrace{-\frac{\hbar\Delta}{4}\left(\frac{\nabla|\Omega|^2}{\Delta^2+\Gamma^2/4+\Omega^2/2}\right)}_{\text{reactive force}} + \underbrace{\frac{\Gamma}{2}\hbar\nabla\phi\left(\frac{\Omega^2}{\Delta^2+\Gamma^2/4+\Omega^2/2}\right)}_{\text{dissipative force}}. \tag{3.9}$$

Now that we have brought the light forces into a form that is more comfortable to work with as expressed in experimental parameters more intuitive to us, let us look into the different force terms individually.

Dipole Force

The first thing that we notice about the reactive force term is its conservative character. The fact that we can write the force as in terms of $\nabla|\Omega|^2$ tells us that the potential is path-independent and therefore dissipation is not present. Surely, if the Rabi-frequency is constant in space e.g. a plane wave, the conservative force will not be present. In the limit of far detuning where $\Delta \gg \Omega$, we get the dipole force [59]

$$F_{dip} = -\hbar\frac{\nabla|\Omega|^2}{4\Delta}. \tag{3.10}$$

In the case of red detuning ($\Delta > 0$), we see that a potential minimum exists at the highest intensity. For blue-detuning, the force will be repulsive. Thus, one can use the dipole force for trapping atoms, molecules [60–62] or even macroscopic [63] objects. It is worthwhile mentioning that the second term in equation (3.9) scales with $1/\Delta^2$ and thus will be neglected for large detuning. Of practical relevance for the implementation is the potential depth of the dipole trap in comparison to the scattering rate. While the dipole force potential scales with $|\Omega|^2/\Delta$, the scattering rate goes as $|\Omega|^2/\Delta^2$. Thus, one should choose very high detuning as long as one can provide enough intensity. Using the dipole force to trap or even manipulate atoms [64] is powerful tool but one needs to get the atoms to a trappable temperature first.

Scattering Force

As already mentioned, the dipole potential will vanish in the case of a plain wave. For this scenario, we have that $\nabla\phi = \mathbf{k}$. Equation (3.3) can after some algebra be written as

$$F_{spon} = \frac{\Gamma}{2}\hbar\mathbf{k}\cdot\rho_{22}. \tag{3.11}$$

It follows that the spontaneous force depends on the linewidth, the recoil momentum and the population. This dependence can be understood in an intuitive fashion. If the atom was excited in a purely stimulated fashion, there would be no momentum transfer as the deexcitation will be in the same direction as the excitation. In average, the spontaneous decay is not directed and therefore momentum transfer occurs in the direction of the laser beam. Smaller lifetimes are associated with a bigger linewidth and therefore a faster rate of momentum transfer. The population plays a role since more efficient transfer of atoms into the excited state results in a higher probability

for a spontaneous decay. We can define a saturation parameter

$$s = \frac{\Omega_0^2/2}{\Delta^2 + \Gamma^2/4} = \frac{I/I_s}{1 + 4\frac{\Delta^2}{\Gamma^2}} \tag{3.12}$$

were I is the intensity and I_s is the saturation intensity ($I_s \approx 1-10\,mW/cm^2$ for alkali atoms). This representation of the saturation parameter is useful when working with lasers. Equation (3.11) can be simplified to

$$F_{spon} = \frac{\Gamma}{2}\hbar\mathbf{k}\frac{s}{s+1}. \tag{3.13}$$

In the limit of $\frac{s}{s+1} \longrightarrow 1$ for infinite intensity, $F_{spon} \longrightarrow \frac{\Gamma}{2}\hbar\mathbf{k}$. This dissipative scattering force can be used to cool and trap atoms.

3.2 Zeeman Slower

In order to quickly and efficiently trap a thermal distribution of atoms originating from an oven, pre-cooling is needed. The problem with laser-cooling a thermal distribution of atoms is that different velocity classes will see a different detuning given by

$$\Delta' = \Delta_{Laser} + \mathbf{kv} - \frac{\mu' B}{\hbar}, \tag{3.14}$$

where the condition for resonant cooling is given by $\Delta' = 0$. With no detuning, we maximize the spontaneous force and therefore also the deceleration. Once atoms are being slowed down, the change in the Doppler-shift will cause a detuning unless the detuning of the laser or the magnetic field is changed simultaneously. In practice, the two most common ways are changing the laser detuning as a function of time or having a spatially dependent magnetic field [5]. The second option can be realized with with a Zeeman slower.

The Zeeman slower allows us to cool velocities up to a critical velocity v_c. The fastest atoms are being cooled once they see a magnetic field of:

$$B_0 = (\Delta_{Laser} + \mathbf{kv_c})\frac{\hbar}{\mu'}, \tag{3.15}$$

where μ' is the magnetic moment of the transition. Once the atoms become slower, they are kept in resonance by decreasing the magnetic field. One can write the magnetic field as a function of propagation distance z along the beam axis which is given by

$$B(z) = \frac{\hbar}{\mu'}\left(\Delta_{Laser} + k\sqrt{v_c^2 - 2az}\right). \tag{3.16}$$

where the a is a constant deceleration. Atoms faster than v_c will not be cooled. Atoms with velocity $v < v_c$ will be resonantly cooled starting from $z = \frac{v_c^2 - v_0^2}{2a}$ where the

maximal deceleration is limited by $a_{max} = \frac{\hbar k \Gamma}{2m}$. At the end of the Zeeman-slower, the atoms will mostly be cooled into one velocity class, cold enough to be captured and further cooled by the magneto-optical trap.

3.3 Magneto-Optical Trap

The MOT is a trapping and cooling method for neutral atoms. The atom can be trapped by driving transitions between hyperfine states with circular polarized light that are shifted in the presence of a magnetic field. The simultaneous cooling is done by the same beams by means of Doppler cooling. The method has been demonstrated at Bell Laboratories in 1987, where temperatures of 600 μK have been achieved [8]. Still today, the MOT is used in most experiments with ultracold atoms.

Optical Confinement - Restoring Force

In contrast to a dipole trap, the MOT consists of near-resonant counter-propagating laser beams. Although the Optical Earnshaw theorem[1] prohibits optical trapping only by means of spontaneous scattering force, the spatial coupling to hyperfine states allows for optical confinement. The confinement can be created with the help of magnetic fields. For the sake of simplicity, let us consider the case of a simplified atom cooled on the transition from $F = 0$ to $F = 1$. Imagine the transition for an atom from a ground state of $|F = 0, m_F = 0\rangle$ to $|F = 1, m_F = -1, 0, 1\rangle$. In the presence of a magnetic field the $F = 1$ manifold will be split. For a weak magnetic field only the linear Zeeman shift of $\Delta E = \mu g_F m_F B$ is relevant and also sufficient for this discussion. If the light is non-resonant with $|0, 0\rangle \rightarrow |1, 0\rangle$, the transition with the other two hyperfine states will become resonant for the appropriate magnetic fields. In the figure below, $|0, 0\rangle \rightarrow |1, -1\rangle$ becomes resonant for some value $z > 0$ and $|0, 0\rangle \rightarrow |1, 1\rangle$ for a value $z < 0$. If the atoms are at the position where the light is resonant, they will experience a force towards the center of the trap which effectively generates a restoring force.

Doppler Cooling - Damping Force

Doppler cooling relies on the spontaneous scattering force of counter-propagating beams. The resulting force will have contributions from each of the individual beams. An atom moving in this configuration with velocity $\mathbf{v}$ will experience a detuning $\Delta - \mathbf{kv}$. Thus, one term in the force with have a $\Delta - kv$ contribution and the other one will have a detuning of $\Delta + kv$ such that the effective force acting on the atom is given by

$$F_{Doppler} = \frac{\hbar k \Gamma}{2} \frac{I}{I_s} \left(\frac{1}{1 + 4(\Delta - kv)^2/\Gamma^2} - \frac{1}{1 + 4(\Delta + kv)^2/\Gamma^2} \right). \tag{3.17}$$

[1] The Optical Earnshaw theorem states that spontaneous force alone cannot lead to a stable equilibrium [65]

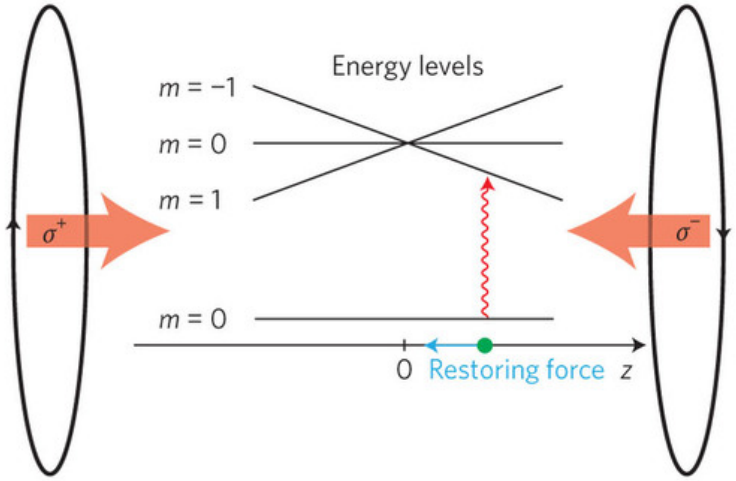

Figure 3.1 – Working principle of magneto-optical trap. The coils are in the anti-Helmholtz configuration and the arrows indicate the propagation direction of the beams, shown only for one axis. The plot displays the energy-levels diagram for a hypothetical atom going from $F = 0$ to $F = 1$. The red wiggly line depicts the transition from the state $|0,0\rangle$ to $|1,-1\rangle$ in the presence of σ^- polarized light accompanied with a photon-kick into the direction of the trap center. The blue arrow on the z-axis represents the direction of the restoring force.

This term can be linearized around zero velocity. This results in a friction-like term (for $\Delta > 0$) of the following form

$$F_{fr} = -8\hbar k^2 \frac{\Delta}{\Gamma} \frac{I/I_s}{1 + (2\Delta/\Gamma)^2} \cdot v, \tag{3.18}$$

often called optical molasses [66].

The friction-like force cools the atoms but not to arbitrary low temperatures. As for every dissipative process, fluctuations are involved that lead to heating. There are fluctuations in the photon momentum from the spontaneous decay and also in the direction that the atoms absorb photons from. For very slow atoms ($\Delta_{Doppler} \sim \Gamma$), one can even speak of a random walk in momentum space. The balance between cooling and heating can heuristically be written as

$$k_B T = \frac{D}{\alpha_{fr}}, \tag{3.19}$$

where D describes the diffusion in momentum space. While on average a random walk in momentum space will lead to zero momentum, the standard deviation is non-

zero and can be described by the diffusion. In fact, for an atom in a light field, the diffusion constant is proportional to the lifetime of the atom in the excited state [67]. The lowest temperature for Doppler cooling, called Doppler temperature T_D, occurs for $\Delta = \Gamma/2$ (see equation (3.18)) leading to $T_D = \frac{\hbar\Gamma}{2k_B}$. In potassium, this corresponds to 145 µK for the D1 and the D2 line.

3.4 Grey Molasses

Grey Molasses is a sub-Doppler cooling technique that combines Sisyphus cooling [68] with a velocity-dependent coupling which has been performed experimentally for the first time with cesium [69]. In order to understand the working principle of the grey molasses, let us first turn towards Sisyphus cooling.

Sisyphus Cooling

The first sub-Doppler cooling scheme that was unknowingly employed was Sisyphus cooling. It came as a surprise to the laser cooling community in the late '80s to observe temperatures below the Doppler limit. As a result, models were developed to explain this behavior [68, 70]. The key features that allow for sub-Doppler cooling are the multilevel character of atoms in combination with a polarization gradient [68].

A toy model for Sisyphus cooling is depicted in Fig. 3.2a. We consider an atom that has two ground state levels $m_J = -1/2$ and $m_J = 1/2$. This atom moves in a polarization gradient that is made up of two counter-propagating beams with linear and orthogonal polarizations (known as lin $\perp$ lin). At different positions along the beam axis, the polarization will change between circular and linear polarizations as indicted in the figure. The transition of the atom will be from $J = 1/2$ to $J = 3/2$. $J = 3/2$ is represented by the dashed line to indicate that further resolution of the level structure is not needed for the discussion.

Let us assume the atom to be in the state $|1/2, -1/2\rangle$ with a velocity $\mathbf{v}$ at the position of σ^--polarized light. With this velocity the atom moves in the polarization landscape. The change in the polarization is connected to a light shift. According to our toy model seen in Fig. 3.2a, the light shifts have the same magnitude and are opposite in sign. This does not have to be the case and is subject to the polarization, the specific transitions, the detuning and intensity of the lasers. During its motion towards a position with σ^+ polarization, the atom gains potential energy. Additionally, as the contribution of σ^+-polarized light grows, so does the probability for the atom to be optically pumped into the state $|1/2, 1/2\rangle$. The aforementioned process represents the conversion of kinetic to potential energy through the changing light shift and irradiation of the potential energy through optical pumping, making up one cooling cycle. Consecutive cooling cycle lead to an effective damping force on the atom.

In order to compare the temperature limits of Doppler and sub-Doppler cooling,

we need to resort to equation (3.19). In this discussion, we will only regard dependencies and do not reproduce the exact form. The friction coefficient can intuitively be understood from the following consideration. The cooling cycle is the most efficient if one cooling cycle happens over the distance of $\lambda/4$. In this case the atom gains the most potential energy before ending up in the low-lying ground state. The potential energy gain would correspond to the light shift ΔE, which for large detuning is given by equation (3.10). The potential energy gain happens over a characteristic time $t \sim 1/\Gamma$. Therefore we can write [68]

$$\frac{dW}{dt} = -F \cdot v = -\alpha_{fr} \cdot v^2. \tag{3.20}$$

It follows that

$$\alpha_{fr} \sim -\hbar k^2 \frac{\Delta E}{\Gamma_{eff}}. \tag{3.21}$$

In the case of large detuning ($\Delta \gg \Gamma$), we can tune the level shift to be larger than the linewidth ($\Delta E \sim \Omega^2/\Delta$, $\Gamma_{eff} \sim \Gamma\Omega^2/\Delta^2$) and in the case of low power ($\Omega \ll \Gamma$), equation (3.21) turns into

$$\alpha_{fr} \sim -\hbar k^2 \frac{\Delta}{\Gamma}. \tag{3.22}$$

The diffusion term D remains proportional to the decay rate Γ_{eff}. This will eventually give us the following relation

$$k_B T \propto \frac{\Omega^2}{\Delta}. \tag{3.23}$$

Equation (3.23) tell us that for a larger detuning and lower powers, the reachable temperature can be reduced arbitrarily. In practice, temperatures orders of magnitude below the Doppler limit and multiples of the recoil temperature $T_{recoil} = (\hbar k)^2/(2mk_B)$ have been achieved. Once, the regime is reached where single photons become relevant, the semi-classical treatment is not valid anymore and a full quantum mechanical approach is needed to determine the cooling limit.

At this point, we can turn to an order of magnitude calculation for the capture velocity. As we already mentioned, the atom picks up the biggest potential energy if it moves through $v_c/\Gamma_{eff} \sim \lambda/4$ before decaying into the other ground state. It follows that

$$k v_c \sim \Gamma_{eff}. \tag{3.24}$$

In contrast to that, the capture velocity of the MOT, referring to the velocity regime of molasses cooling, is determined by $k v_c = \Delta$.

The essential information of our calculation is that the temperature limit and the capture velocity are much lower for sub-Doppler cooling than for Doppler cooling. For all practical purposes, Doppler cooling is essential to reach a velocity regime for

sub-Doppler cooling.

With Sisyphus cooling it is possible to reach sub-Doppler temperatures. The need for the grey molasses can be questioned if Sisyphus cooling turns out to be so successful. A very practical reason is that the temperatures that were reached with the grey molasses for Potassium-39 [71] are four times lower than other polarization gradient cooling schemes [72] which are limited by photon reabsorption [73].

Grey Molasses - Simplified Cooling Mechanism

Grey Molasses, as an alternative sub-Doppler cooling approach has already been demonstrated for cesium and rubidium nearly two decades ago [69, 74].

In Fig. 3.2b, a simplified example for grey molasses is depicted where the states are not necessarily hyperfine states and denoted as "dark" and "bright". An atom in the dark state is being transferred into the bright state through motional coupling. Once in the bright state, the atom moves up the potential hill caused by a polarization or intensity gradient and, just as for Sisyphus cooling, kinetic energy is converted into potential energy before the atom decays back into the dark state. During this process, the probability to be optically pumped back into the dark state increases where one cooling cycle is completed. In the following, we discuss the emergence of the dark states, how the dark and bright state couple motionally and the differences to Sisyphus cooling with the aim to get a better understanding for the grey molasses and why it works in a three dimensional setup beyond the simple toy model.

Dark States

Dark states in the sub-Doppler cooling scheme can arise from two different effects. One of the possibilities is that a forbidden dipole transition renders a state to be dark. This usually happens for a specific polarization. For an excitation from $|F\rangle \rightarrow |F\rangle$ or $|F\rangle \rightarrow |F-1\rangle$ and sigma polarized light a dark state will be present. To be specific, let us consider $|F, m_F = \pm F\rangle$. In the case of $\sigma^{\pm}$, the state cannot couple. The second possibility is that a dark state can occur due to two hyperfine sub-states $|1\rangle$ and $|2\rangle$ that couple to an excited state $|3\rangle$. In the dressed picture, the states $|1\rangle$ and $|2\rangle$ can be rewritten into the following form

$$|\text{Dark}\rangle = \frac{\Omega_2|1\rangle - \Omega_1|2\rangle}{\sqrt{\Omega_1^2 + \Omega_2^2}} \quad \text{and} \quad |\text{Bright}\rangle = \frac{\Omega_2|1\rangle + \Omega_1|2\rangle}{\sqrt{\Omega_1^2 + \Omega_2^2}}, \tag{3.25}$$

where Ω_i are the Rabi frequencies for the state $|i\rangle$. For this discussion, it does not matter whether the states lie in the same hyperfine manifold or not. In the end, a three-level system that fulfills the Raman condition, namely that the two relative detuning between the transition $|1\rangle \rightarrow |3\rangle$ and $|2\rangle \rightarrow |3\rangle$ is zero, exhibits a dark state. Sub-Doppler cooling schemes that make use of two states that come from different hyperfine manifolds are often referred to Λ-enhanced, while the underlying physics does not change. However, it is of importance which type of dark state one employs

in the setup. In order to be independent of the polarization, we are interested in the dark states that arise from a three-level system.

Without going into the theory of three-level systems, we write down the light-atom interaction Hamiltonian in the rotating frame:

$$\hat{H}_{LA} = \frac{\hbar\Omega_1}{2}|1\rangle\langle 3| + \frac{\hbar\Omega_2}{2}|2\rangle\langle 3| + c.c. \tag{3.26}$$

From the Hamiltonian it becomes evident that the dark state does not couple to the bright state and furthermore, the dark state does not couple to couple to light, leading to the absence of a light shift. If the coupling between the dark and the bright state is absent, we need to explain how the atom can be transferred into the bright state.

Motional Coupling

The coupling between the dark and the bright state arises from motional coupling and not from optical pumping which is the case for Sisyphus cooling. Besides the light-atom interaction, we can introduce the kinetic energy term into our Hamiltonian $\hat{H}_{KE} = \hat{p}^2/2m$. Once we introduce the motional degrees of freedom into our description, we will have to rewrite the bright and dark states to take the following form [75]

$$|\text{Dark}\rangle = \frac{\Omega_2|1, p - \hbar k\rangle - \Omega_1|2, p + \hbar k\rangle}{\sqrt{\Omega_1^2 + \Omega_2^2}} \tag{3.27}$$

and

$$|\text{Bright}\rangle = \frac{\Omega_2|1, p - \hbar k\rangle + \Omega_1|2, p + \hbar k\rangle}{\sqrt{\Omega_1^2 + \Omega_2^2}}. \tag{3.28}$$

Still, $\langle 3, p|\hat{H}_{KE} + \hat{H}_{LA}|\text{Dark}\rangle = 0$ but $\langle\text{Bright}|\hat{H}_{LA}|\text{Dark}\rangle \neq 0$. This is simply a result of $\hat{H}_{KE}$ not being diagonal in the basis of the states. A simple calculation shows that

$$\langle\text{Bright}|\hat{H}_{KE}|\text{Dark}\rangle = -\hbar\frac{2\Omega_1\Omega_2}{\Omega_1^2 + \Omega_2^2}\frac{pk}{m}. \tag{3.29}$$

Thus, we reach a coupling between the bright and the dark state that scales with the velocity while the dark state does not experience a light shift. The dark state becomes "truely" dark for the motional coupling, once the atoms at zero velocity. According to [75], the motional transition probability scales with the square of the velocity and inversely with the light shift of the bright state. Given that the transition probability for the bright state increases with the light shift, it is ensured that the atoms lose kinetic energy.

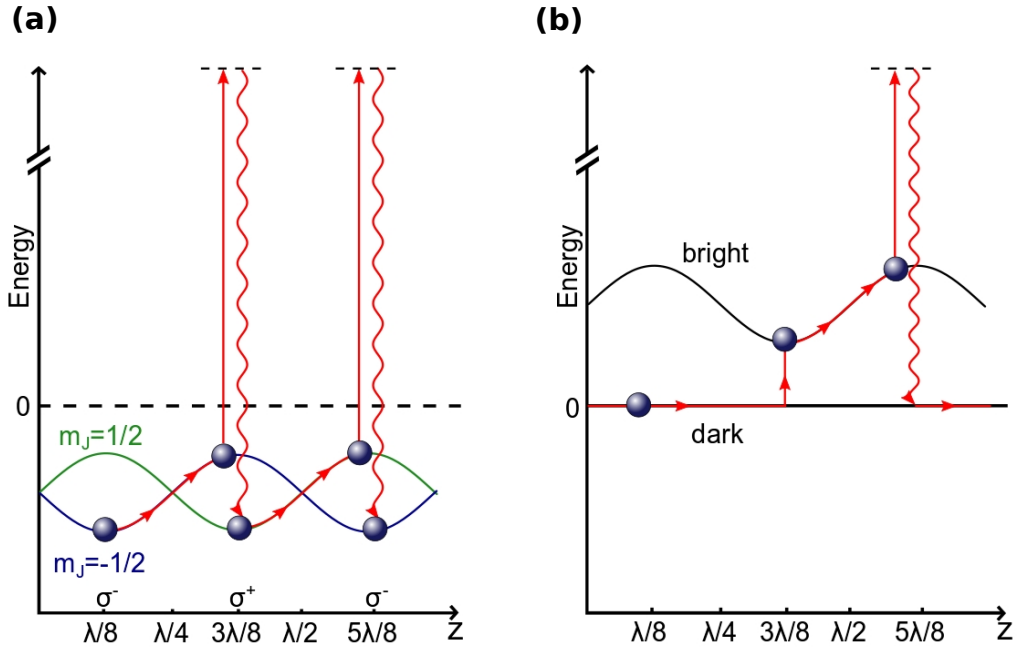

Figure 3.2 – Sisyphus cooling and grey molasses. Comparison between Sisyphus cooling and grey molasses. The horizontal axis depicts the distance and the according polarization while the vertical axis marks an arbitrary energy scale. **a** Two ground states are present. Both of them couple different to the light according to the polarization. If a moving atom is initially in the state $m_J = -1/2$, it will gain potential energy by moving to a position of stronger coupling. There, it will be transferred to an excited state and spontaneously decay into $m_J = 1/2$ where it will repeat the procedure resulting in continuous loss of kinetic energy. **b** The dark state does not exhibit any position dependent light shift. An atom in the dark state will have a velocity and light-shift dependent coupling to the bright state. Just like for Sisyphus cooling, the atom will move up a potential hill from where it decays into the dark state through optical pumping. Image adapted from [76].

CHAPTER 4

Experimental Setup

The experimental realization to cool potassium to sub-Doppler temperatures is subject of this chapter. At first, the properties of potassium, especially Potassium-39, will be presented. This will set the basis to discuss the optics setup for laser cooling. We will start with a general discussion of the laser setup before it will be presented in full detail. This is followed by a characterization of the laser system, being the main topic of this thesis. For completeness and as a reference for future work, the vacuum system will be presented. Based on our findings, we will discuss possible cooling sequences and considerations for their optimization in the last section.

4.1 Properties of Potassium

The fact that potassium is an alkali atom makes it very reactive. It has three natural occurring isotopes where two of them are the stable bosonic isotopes Potassium-39 and Potassium-41, and one long-lived fermionic radioisotope Potassium-40. Potassium has a combination of different properties compared to other alkali that make it the preferable atomic species for this experiment.

Laser cooling - For atoms such as cesium or rubidium, it is harder to derive light for cooling and repumping from the same beam due to the hyperfine splitting of at least several GHz. In the case of potassium, the ground state splitting of 461.7 MHz can be bridged by frequency shifts using acousto-optical modulators, simplifying the optical setup.

UV-Laser - A high power laser system to generate UV-light for potassium is considerably easier than in the case for lithium, the only other alkali with a fermionic isotope, where the ionization wavelength is around 230 nm.

Double Rydberg dressing - The ground state splitting allows us to encode spin systems through the two dressed hyperfine ground states.

Microtraps - The loading of microtraps with unity-filling might be more efficient for potassium than for rubidium. There are arguments that suggest that larger light shifts in potassium increase the probability for the blue shielding [77] to be effective.

Isotope	Nat. abundance [%]	Mass [u]	Lifetime [y]	Nuclear spin
^{39}K	93.2581(44)	38.96370668(20)	stable	3/2
^{40}K	0.0117(1)	39.96399848(21)	1.28 x 10^9	4
^{41}K	6.7302(44)	40.96182576(21)	stable	3/2

Table 4.1 – Basic properties of the three natural occurring isotopes in potassium. This table, adapted from [78], summarizes the most basic properties for the three potassium isotopes of interest.

Property	Symbol	Value
Saturation intensity	I_{sat}	1.75 mW/cm^2
Optical properties D1		
Frequency	ν	389.286058716(62) THz
Wavelength	λ	770.108385049(123) nm
Natural linewidth	Γ	5.956(11) MHz
Recoil velocity	v_{rec}	1.329825973(7) cm/s
Recoil temperature	T_{rec}	0.41436702 µK
Doppler temperature	T_D	145 µK
Optical properties D2		
Frequency	ν	391.01617003(12) THz
Wavelength	λ	766.700921822(24) nm
Natural linewidth	Γ	6.035(11) MHz
Recoil velocity	v_{rec}	1.335736144(7) cm/s
Recoil temperature	T_{rec}	0.41805837 µK
Doppler temperature	T_D	145 µK

Table 4.2 – Optical properties of Potassium-39. The relevant optical properties for the D1 line and D2 line in Potassium-39. The information in this table has been taken from [78].

Optical Properties of Potassium-39

Like all alkali, potassium can be seen as a hydrogen-like atom with a more massive nucleus. The energetically lowest lying transitions in Potassium-39 are called the D lines in the infrared. These transitions are used in our laser cooling schemes. Due to the coupling of the nuclear spin **I** to the total electronic angular momentum **J**, there is a hyperfine splitting. One can define a new quantum number $\mathbf{F} = \mathbf{J} + \mathbf{I}$. From the addition of angular momenta, we know that $|I - J| \leqslant F \leqslant |I + J|$ [79]. Since $^2\mathbf{P_{1/2}}$ and $^2\mathbf{S_{1/2}}$ both have $\mathbf{J} = 1/2$, we expect a two-fold splitting with $\mathbf{F} = 1, 2$. In the case of the D2 line, the excited state can be split into four hyperfine states due to $\mathbf{J} = 3/2$. The level diagram for the fine states and hyperfine states can be seen in Fig. 4.1.

The transition strengths, as depicted in [67], indicate that laser cooling will be preferable on the D2 line than on the D1 line. Using circular polarized light on the D2 transition will lead to at least three times stronger coupling. Additionally, the transition from $|F = 2, m_F = \pm 2\rangle$ to $|F' = 3, m_{F'} = \pm 3\rangle$ will be the most closed

transition. Since the grey molasses cannot be performed on the D2 line, the same considerations need to made on the D1 line. As the transitions strength between $|F = 2, m_F = 2\rangle$ to $|F' = 2, m_{F'} = 2\rangle$ and $|F = 2, m_F = 2\rangle$ to $|F = 2, m_{F'} = 1\rangle$ is comparable, a strong repumper will be needed.

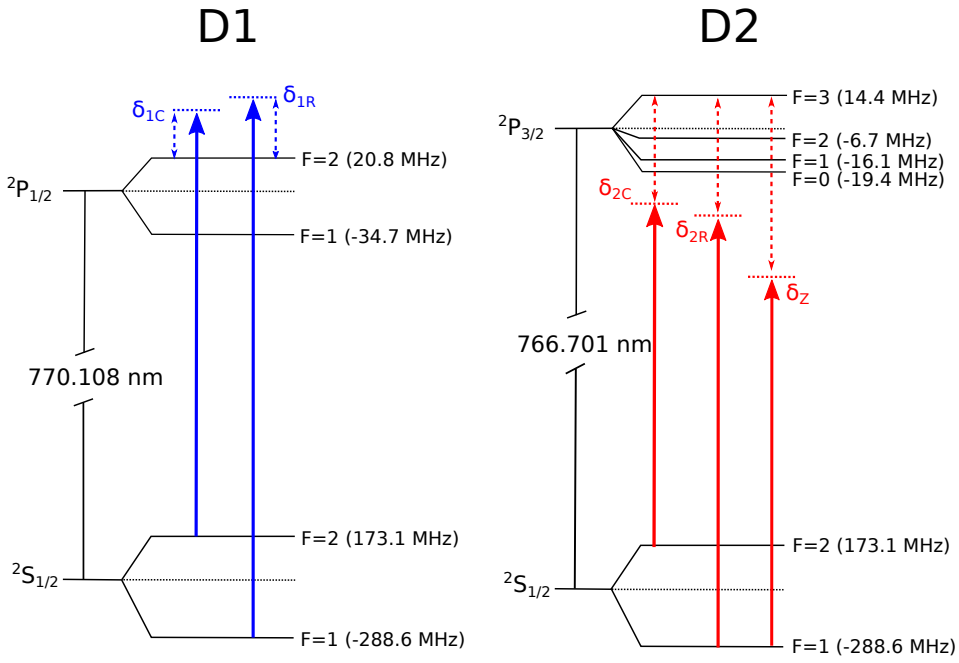

Figure 4.1 – Level structure in Potassium-39. The level structure for the D1 line and D2 line in Potassium-39. The wavelength for the D lines are indicated. The black dashed line represents the fine states and serves as a reference. The blue and red arrows indicate the laser frequencies for the transitions used for laser cooling. The specific detunings will be summarized and discussed in 4.4 and 4.5.

4.2 Laser Cooling Setup

The setup for laser cooling built during this thesis is intended to cool Potassium-39 to sub-Doppler temperatures. Temperatures of 10 µK at a phase-space density (PSD) of $2 \cdot 10^{-4}$ have already been achieved in several similar setups such as [71]. Such temperatures and phase-space densities are a good starting point to load atoms into dipole traps, either to cool them further by evaporative cooling or to perform experiments with "hot" atoms in microtraps.

A possible outline to reach such temperatures and PSDs is to decelerate the atoms from a thermal distribution at 100°C inside a Zeeman slower to a velocity of a few meters per second, reducing the temperature of the sample to about 150 µK inside the magneto-optical trap. After that, the compressed MOT (CMOT) with a stronger magnetic field gradients can be applied, followed by the grey molasses cooling scheme

which allows the sample to reach sub-Doppler temperatures.

To realize such a cooling sequence, the laser setup needs to fulfill various criteria. Since we are cooling on different D lines, we require at least two different lasers and without closed transitions, we need to have cooling and repumping beams. Considering the power balances at other experiments such as [80], we will need around $240\,mW$ of power for all cooling beams. Comparable values will be needed for the repumper. For the different cooling stages, we will require to adjust the detunings. Thus, we need to be able to control and tune the laser frequencies of each individual beam while retaining sufficient laser power. A simplified version of the setup can be seen in Fig. 4.2.

The setup contains three lasers, two of which are for the cooling of Potassium-39 to reach sub-Doppler temperatures, while the Image-Laser allows us to image our atomic cloud. All lasers are locked to a spectroscopy cell, enabling us to determine and stabilize the laser frequency. While only a few milliwatts of power are needed for the imaging, the MOT-Laser and the GM-Laser need to be amplified by means of a tapered amplifier. After the amplification, we split the beams from the MOT-Laser and the GM-Laser to derive the cooling and repumping beams. The beam for the Zeeman slower also originates from the MOT-Laser. To be able to control all the beams individually in frequency and amplitude, AOMs are implemented in the setup. The AOMs allow tunability and switching of individual beams. Beam shutters are an additional mean to gate all beams independently. After the AOM paths, the cooler and repumper beams are recombined and then coupled into a fiber. Since we want to image and cool on all axes, three fibers are needed. The fibers lead to the experimental table where they are guided to the vacuum chamber. For details of the full optical setup, see Fig. 4.3 and Fig. 4.4.

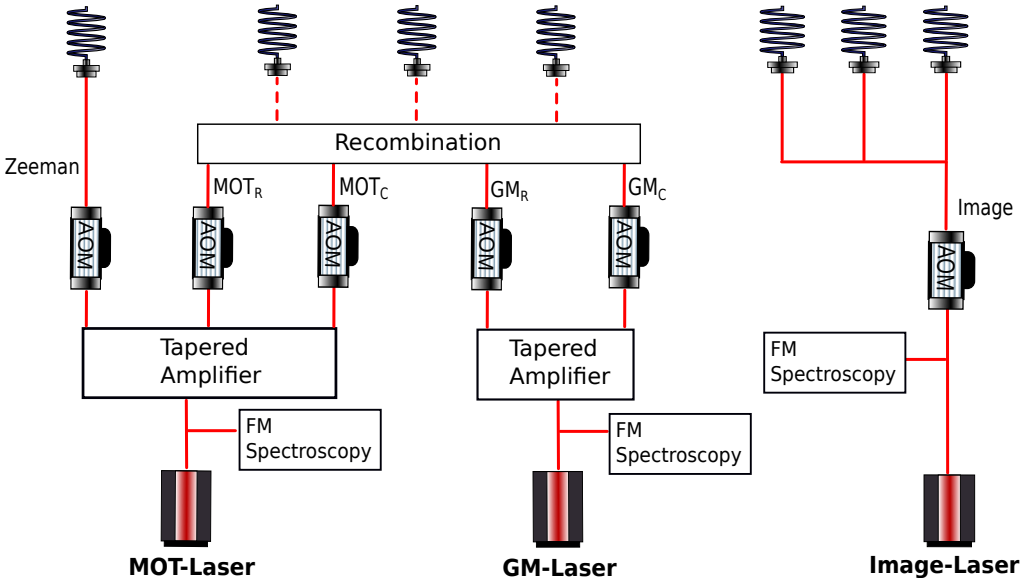

Figure 4.2 – Simplified optics setup for Doppler and sub-Doppler laser cooling. Three lasers are locked by FM spectroscopy to a crossover transition. The Image-Laser is sent into three different fibers after being detuned by an AOM. The MOT-Laser and GM-Laser are amplified by a tapered amplifier. After the amplification, the beams are divided and detuned. A recombination path is required to combine the four different beams for the MOT and grey molasses before being sent into three fibers.

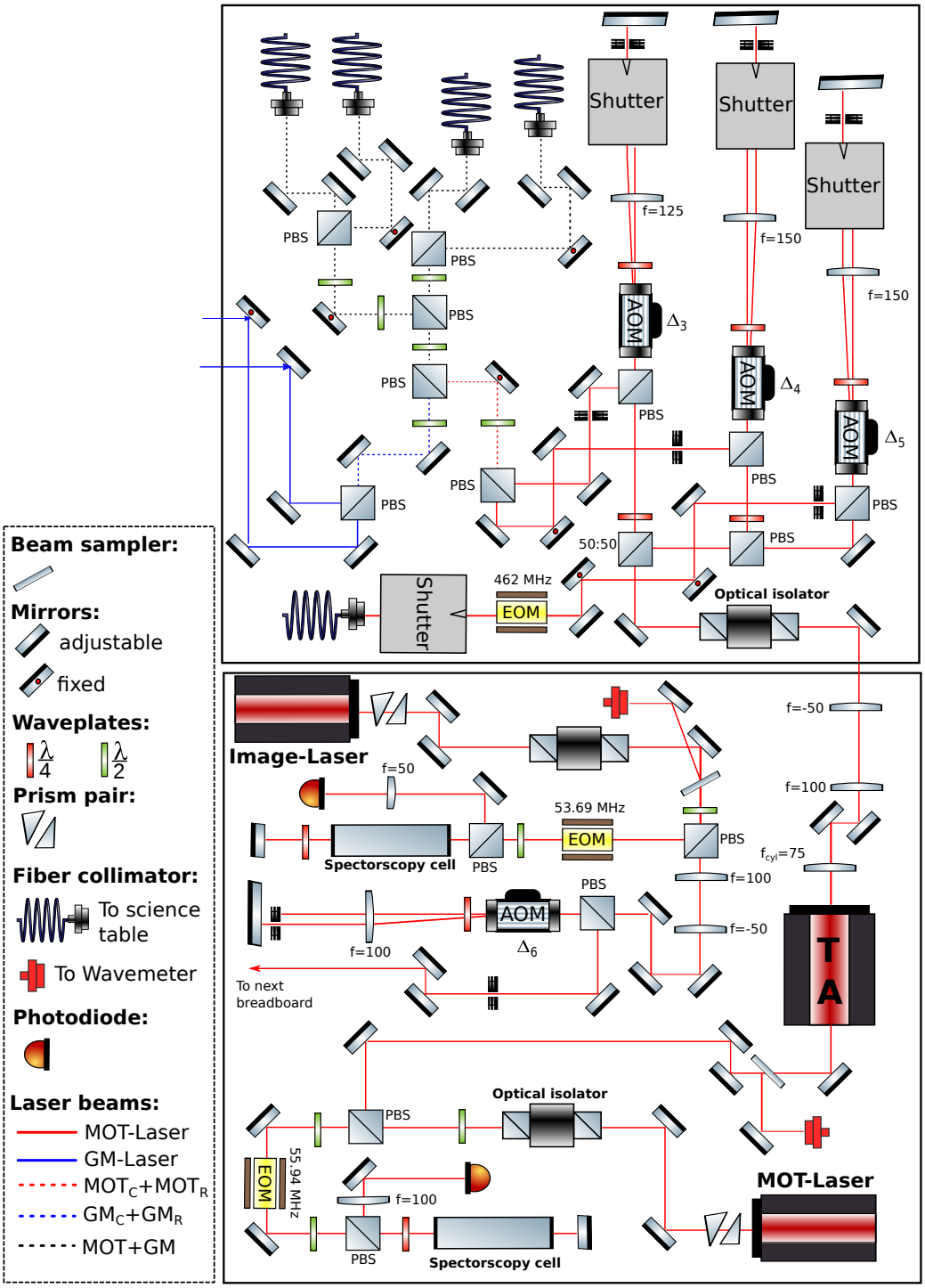

Figure 4.3 – Breadboards with MOT-Laser, Image-Laser and recombination. The MOT-Laser and the Image-Laser both are locked to a spectroscopy cell. The MOT-Laser is amplified and sent to the upper board while the Image-Laser is detuned with an AOM and sent to the lower board seen in Fig. 4.4. The MOT-Laser is then split into the cooler (MOT_C) and repumper (MOT_R) for the MOT and the Zeeman slower ($Zeeman$). The beams for the MOT and grey molasses are recombined and coupled into fibers.

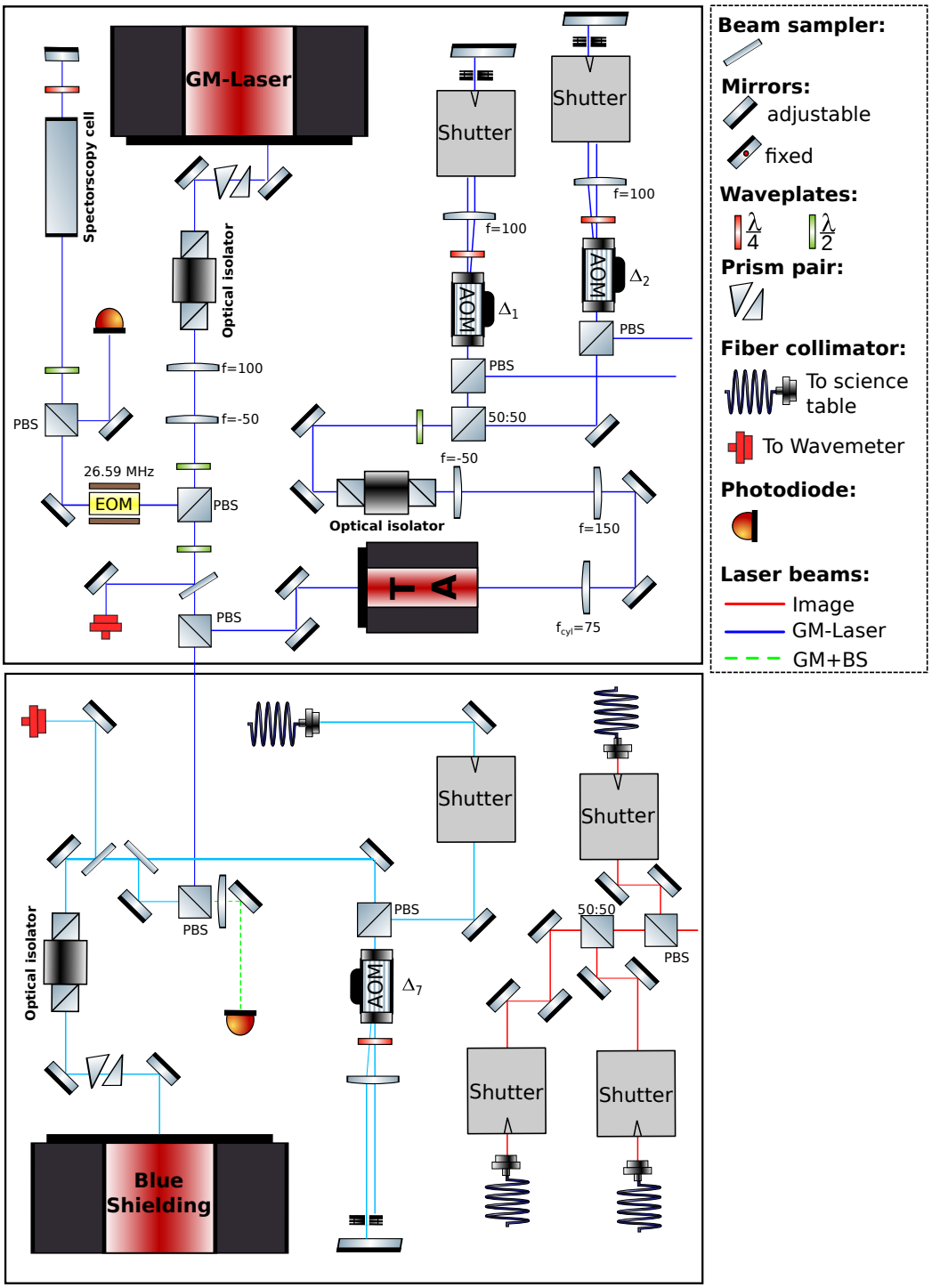

Figure 4.4 – Breadboards with the GM-Laser, the Blue Shielding-Laser and fiber coupling of Image-Laser. On the upper board one can see the locking of the GM-Laser, the amplification of the light and how the cooler (GM_C) and the repumper (GM_R) are generated and sent to the other board in Fig. 4.3 for the recombination. On the lower board, one can see how the Image-Laser is divided. For completeness, the laser for the blue shielding is depicted which is offset-locked with respect to the GM-Laser.

4.2.1 Lasers

The external cavity diode lasers (ECDL) used in our setup for laser cooling are self-built. The interference-filter-stabilized [81] laser, called linear laser, has feedback through a low-reflectivity mirror while the Littrow-type laser generates feedback through a diffraction grating. All lasers are controlled by a current controller (Thorlabs LDC202C) and a temperature controller (Thorlabs TED200C). In order to prevent wrong polarity on the laser diode and to decouple modulations from the controller, the laser diode is connected through a protection board, designed by a former Master's student.

Linear Laser

The linear lasers (see Fig. 4.5) are used for the D2 transitions in our setup. This includes the imaging and the MOT light. The light that comes out of the laser diode passes through an interference-filter (etalon) and gets focused by a lens onto a mirror that has been mounted on a piezoelectric actuator (piezo). In essence, the laser has two different resonators, one being the etalon which serves as a coarse selection of the wavelength while the mode is determined by the cavity between the laser diode and the mirror. The light that passes through the mirror is collimated by a second lens and transverses a window.

The optimization of the output power, as well as the wavelength, can be done individually. It is advised to first optimize the laser power which is easier without the etalon. In the first step, one should try to collimate the output of the laser diode before inserting it into the housing. One then tries to optimize the output power by tilting the mirror holder. For all practical purposes, this is equivalent to reducing the threshold for lasing. After that, the first lens can be moved to focus the light onto the mirror. These processes need to be done iteratively to fully optimize the output power. The resulting powers as a function of the current are shown in Fig. 4.7a. The typical increase in power occurs for the two linear lasers. Although the linear lasers have the same diode, the lasing threshold is considerably different. The reason is that the diode protection boards have different junction gate field-effect transistors (JFETs). The current offset of about 30 mA for the JFETs is in agreement with the different specified zero gate voltage drain currents. During the measurement of the power, it was observed that the image laser has a strong mode-sensitive output power indicated by this seemingly oscillating behavior seen in Fig. 4.7a. After the power optimization, the second lens can be set to re-collimate the beam. The insertion of the interference-filter follows. By tilting it, one can select for the desired wavelength range. With our interference-filter, a wavelength of 766.7 nm can be achieved at tilt of about 6° between the normal of the grating and the laser beam.

To exclude multi-mode operation of the linear lasers, we generated a beat signal between two lasers (given by blue curve in Fig. 4.7). We locked one of the lasers onto the D2 crossover in Potassium-39 while locking the other one to a physical transition on the D2 line. By overlapping the two lasers and sending them onto a photodiode, one gets a DC contribution as well as an AC contribution. From the addition of

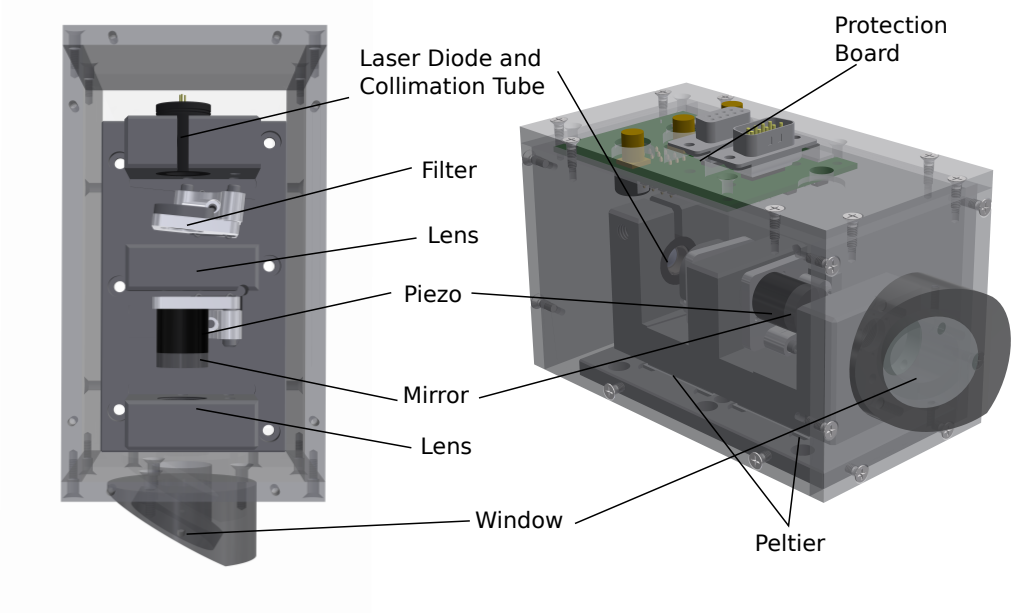

Figure 4.5 – Render of the linear laser. Two different perspectives of the linear laser with its most important elements: laser diode (Eagleyard EYP-RWE-0790-04000-0750-SOT01-0000), piezo (Piezomechanik HPST 150/14-10/12), aspheric lenses (Thorlabs C280TMD-B), etalon (Laseroptik L-05291), low-reflectivity mirror (Laser components PR780/20/AR), Peltiers (RS 490-1480) and a window (Thorlabs WG11050-B). The components are fixed to an E-shaped base. Below the aluminium base, one can see the Peltiers as well as a base plate, also made of aluminium. The housing of the laser is made of acrylic glass to protect the sensitive components as well as to isolate the laser from environmental disturbances.

electric fields, we expect the sum-frequency and the difference-frequency for the two different light fields. The sum frequency lies in the THz and cannot be detected by a photodiode. Instead the difference-frequency around 200 MHz was be measured with a fast photodiode (Hamamatsu G7096) and a low-noise amplifier (Kuhne KU LNA BB 0180 BT). The spectrum analyzer (Anritsu Spectrum Master MS2721B) was used to detect multi-mode operation in which case we would expect a beating signal at the mode separation. The spectrum analyzer only showed one peak at a frequency of about 200 MHz. Besides excluding multi-mode operation, we used the beat signal in order to measure the linewidth of the linear laser.

According to Fig. 4.7b, we can see that two different models have been applied to fit the raw data, a Lorentzian and a Gaussian model. It follows that the beat signal is the convolution of two Gaussian or Lorentzian functions with their respective linewidth of $\Delta L = \Delta L_1 + \Delta L_2$ or $\Delta L = \sqrt{\Delta L_1^2 + \Delta L_2^2}$ [82]. For the Lorentzian model, the linewidth is given by $\Gamma_{\text{Lorentz}} = 157.04 \pm 1.8\,\text{kHz}$. In the case of the Gaussian model, the linewidth is given by $\Gamma_{\text{Gauss}} = 307.22 \pm 2.0\,\text{kHz}$. An assumption that was made for

retrieving these values is that the linewidth of the two lasers are the same. From the plot, we can clearly see that the Gaussian model reproduces the wings of the data. On the other hand, the feature around the maximum are not captured well by the Gaussian model. Since the data is very noisy, it is difficult to determine the precise fitting model. A fit with a Voigt profile almost reproduces the Gaussian profile (and therefore is not shown). We conclude that the more appropriate model for the laser linewidth seems to be a Gaussian resulting from technical 1/f-type noise [83].[1] At this point it is worthwhile mentioning that the beat note was measured for two locked lasers where the lock is not fully optimized. The important result is that a non-optimized lock leads to linewidth far below the natural linewidth.

Even though the beat signal measurement results in a linewidth far below the natural linewidth of the cooling transitions, we can perform another measurement to challenge these results. In contrast to a beat signal, we will now resort to a different technique where the assumption that the linewidths are the same is not required. With an optical spectrum analyzer (Sirah EagleEye), we can lock an individual laser to a low-finesse cavity. The EagleEye measures a transmission signal from the light passing through the cavity and locks it at the full width at half maximum (FWHM). The power noise from the laser on short timescales can be converted into frequency noise providing us with a value for the linewidth. In order to have a representable measurement, one needs to make sure that the fit for the Airy function is updated and that the laser is appropriately coupled into the cavity. We made use of the series measurement provided by the EagleEye collecting at least 80 data points for each laser, unlocked and locked. The results are summarized in Table 4.3. This measurement serves two purposes. Knowing the linewidth of the lasers in the unlocked state is a good reference for quantifying the lock at a later stage. One expects to see a lower linewidth in the case of a tight lock and an even bigger linewidth for wrong locking parameters. Second, we are able to check whether assuming the linewidth of two linear lasers to be the same is justified. For the suitable representation and interpretation of this data a few remarks need to be made:

- At the time of the beat signal measurement, the lock was not quantified and therefore the linewidth can be reduced further. For details on the locking and how the lock was optimized, refer to 4.2.2.
- The EagleEye measurements strongly depend on power fluctuations. In the case of the MOT-Laser and the GM-Laser, the linewidths have been measured after the tapered amplifier which also might induce power noise distorting the measurement.
- The results from the EagleEye can be considered tentative. The frequency drift of unlocked lasers is not accounted for in the EagleEye but is considered for the

[1] Determining which model to apply is not a trivial task. It has been shown that pure white-noise leads to a Lorentzian lineshape studied in [84]. Knowledge of the phase noise spectral density will provide more insight. Measuring this quantity is outside of the scope of this thesis but [85] serves as a practical and instructive guide into this topic.

linewidth calculation. This leads to high uncertainties on the linewidth measurement (see Table 4.3). Seeing that the GM-Laser has the lowest uncertainty and having observed that it drifts less, supports this claim.

The conclusions that we draw from this measurement will remain conservative. We can observe that the linewidth of the laser in the locked and unlocked case is far below the natural linewidth and that the linewidth measurement through the beating and the EagleEye are in the same order of magnitude. The linewidth for the locked lasers is smaller than for the unlocked lasers but they remain within the error bars.

Littrow Laser

The Littrow laser [86] is used for the grey molasses and for the blue shielding on the D1 line. Our design is a modified version that originates in the Steck group at the University of Oregon and has been characterized in [87]. The changes in the design include going from imperial screws to metric screws and also the housing itself. Contrary to the linear laser where the feedback happens through a mirror, the feedback is generated by a diffraction grating. The first order diffraction from the grating is coupled back into the laser diode [86] while the zeroth order constitutes the laser output. The advantage of this design is that one can tune the wavelength when tilting the diffraction grating covering a much larger wavelength range than in the case of the linear laser. These Littrow-type lasers can be evacuated or purged with argon possibly leading to more stability. This will not be investigated in this thesis as it is of less relevance for the laser cooling but might be relevant for the two-photon Rydberg excitation lasers. From Table 4.3, we can extract that even without purging or evacuating, the linewidth of the GM-Laser is comparable to the linear lasers.

In contrast to the linear laser, the control for the wavelength and the optimization of the output power cannot be set independently. Both of these parameters are adjusted by the position of the grating. The grating is fixed to a grating arm which can be tilted around the vertical axis with the grating adjustment screw pushing it. Also, the diode collimation tube can be tilted in the vertical direction with the tilt adjustment screws. In practice, one can even achieve this additional degree of freedom by selecting the position the piezo and sapphire discs are pressing against on grating arm. When the grating lines are perpendicular to the input beam and the first order coincides with the incoming beam, the ideal position is found. The general procedure for setting up the laser is to first tilt the diode such that the polarization is vertical so that the Brewster window transmits the most power. Then one tilts the grating at about 45°. Changing the direction of the diode with the tilt adjustment screws should result in the first lasing. Adjustment of the collimation tube lens, the grating arm and the tilt adjustment should suffice to optimize for power and the right wavelength.

While the multi-mode operation was not a problem in the linear laser, it constitutes a serious issue in the Littrow laser. When getting close to a mode jump, there is a range where the Littrow laser will lase at two different modes, an unfavorable scenario that should be avoided by selecting the mode with care. By changing the current, one can

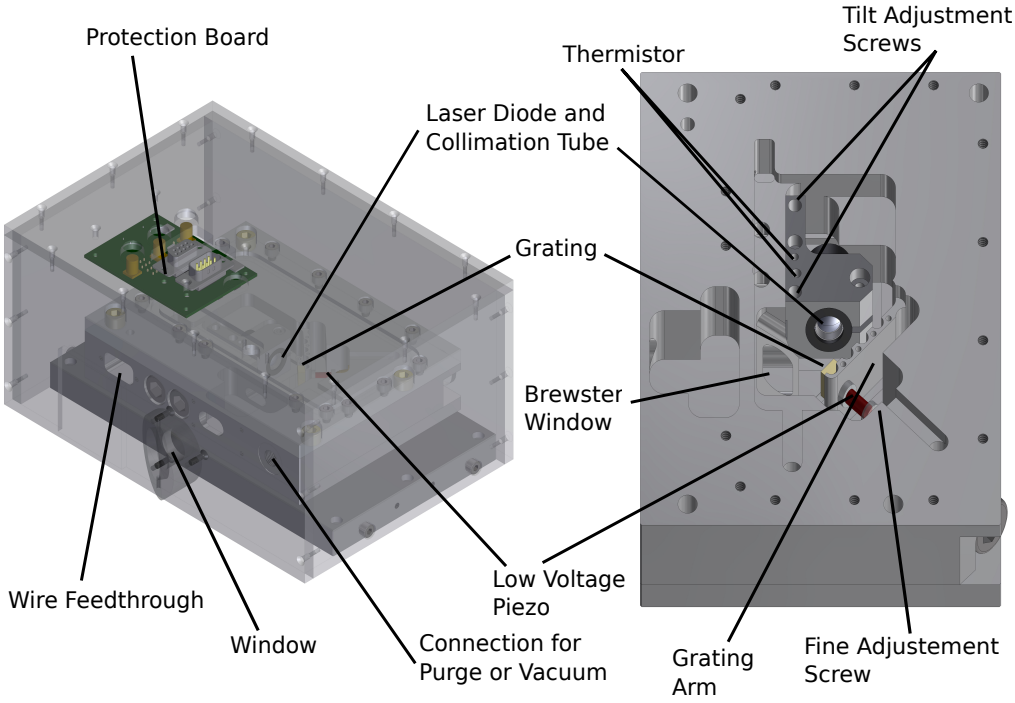

Figure 4.6 – Render of the Littrow laser. Two different views of the of the Littrow laser with its most important elements: the laser diode (Eagleyard EYP-RWE-0790-04000-0750-SOT01-0000), diffraction grating (Richardson Gratings 33A78BK02-33H), adjustment screw (Newport 9376-K), sapphire discs (from SITUS Technicals GmbH) and low-voltage piezo (Piezomechanik PSt150/5x5/7).

set the laser to a stable mode and that is close to the desired frequency. In the next step, one can change the temperature to reach the desired wavelength and simultaneously push the other modes as far away from that frequency as possible. The importance of this will become clear later when the locking of the lasers is discussed where small changes in the piezo or current can push the laser close to a mode jump. The mode selection is solely tuned by the temperature and the current. It is an iterative process and while there is no need to readjust the grating at this stage.

Laser	MOT-Laser	GM-Laser	Image-Laser
Linewidth unlocked [kHz]	263 ± 64	226 ± 26	230 ± 116
Linewidth locked [kHz]	194 ± 39	144 ± 12	105 ± 35

Table 4.3 – Laser linewidths measured by the EagleEye. The MOT-Laser and the GM-Laser linewidths are measured after the tapered amplifiers, AOMs and recombination. In contrast, the Image-Laser light does not pass a tapered amplifier.

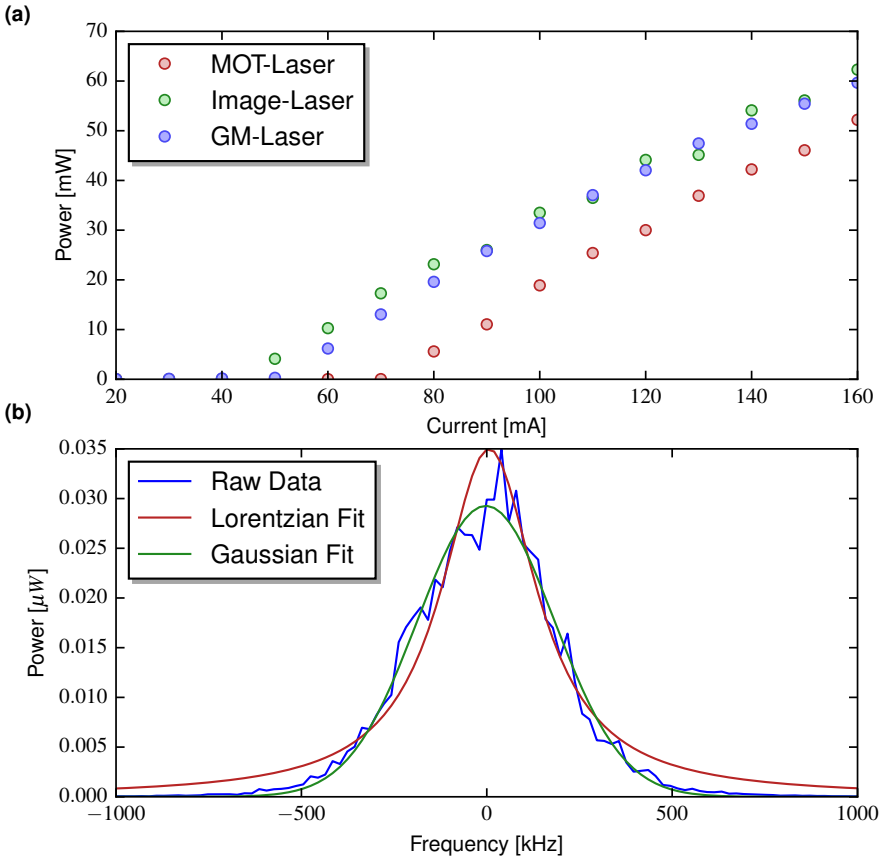

Figure 4.7 – Laser output power and beat signal between linear lasers. **a** Laser power as a function of the current for the MOT-Laser and the Image-Laser. The lasing threshold can be seen when a sudden linear increase in the laser power occurs. **b** Measurement of the linewidth of two different linear lasers with a beating signal. The raw data from the spectrum analyzer can be seen in blue while the fitted curves are given by the red (Lorentzian) and the green (Gaussian) curves. The beating occurs at a frequency of about 200 MHz but is shifted to the origin.

4.2.2 Spectroscopy and Locking

The stability of lasers is crucial for the cooling and trapping of atoms. Drifts in the laser frequency can lead to heating or inefficient cooling. In order to stabilize the laser frequency and to detune it, we need to determine the frequency in the first place. To determine it, one needs a reference. Our wavemeter only has a sensitivity of 100 MHz and thus we make use of a potassium vapor cell. Performing spectroscopy allows us to create a feedback signal, eliminate frequency drifts and reduce the linewidth of the laser.

Saturation Absorption Spectroscopy

A way to find atomic transitions by sending light through a vapor cell. By tuning the laser frequency across a transition, the transmission signal will exhibit dips due

to the absorption by the atoms. The vapor cell needs to be heated and consequently the absorption profile experiences an inhomogeneous Doppler-broadening. It can be described by a Gaussian in one dimension [88] with a FWHM of $\Delta\nu_{Doppler} = \frac{1}{\lambda}\sqrt{\frac{8k_B T \cdot \ln(2)}{m_{^{39}K}}}$ [89]. Our reference cells are heated to about 65°C which results in a FWHM linewidth of approximately 820 MHz. To put this into relation, the hyperfine splitting of the ground state in Potassium-39 of about 460 MHz would still be detectable while the excited states on the D1 line, separated by 55.5 MHz, will not be resolved. Hence, we need to resort to saturated absorption spectroscopy [88].

In saturation absorption spectroscopy, a Doppler-free spectroscopy, we align beams transversing the spectroscopy cell in a counter-propagating configuration as can be seen in Fig. 4.10. By doing so, we see narrow features within the Doppler broadened profile. Without loss of generality, let us consider an atom that has a two-fold ground state and an excited state. This example is representable for the D2 transition where the upper four hyperfine states cannot be resolved and are considered as one transition because the linewidth is comparable to the hyperfine state splitting. The possible transitions from each ground state occur resonantly at a frequency ν_1 and at ν_2. We ramp the laser frequency region that includes ν_1 and ν_2, where we can treat the change in the frequency for the incoming beam, called pump beam, and for the reflected probe beam to be the same. At the frequencies ν_1 or ν_2, we will observe a transmission peak. This transmission peak occurs since the pump laser causes absorption in the atoms for a velocity class $v \approx 0$ and saturates the transition, hence the name saturation absorption spectroscopy. This saturation will not allow for population transfer by probe beam which is possible at other frequencies.

In contrast to a simple two-level system, our three-level scenario will leave us with an additional feature, the crossover transition at the frequency $\nu = \frac{\nu_1+\nu_2}{2}$. For the crossover frequency, the pump beam will induce transitions from the lower ground state to the excited state for atoms blue-detuned atoms and transitions from the higher-lying ground state to the excited state for red-shifted atoms. Since the probe beam is moving in the opposite direction, we can infer that the transitions are crossed. The detuning mentioned is caused by atoms of velocity classes $v = \pm\frac{c}{2}\frac{\nu_2-\nu_1}{\nu_1+\nu_2}$. Although for the same transition the pump beam excites the atoms with velocity $v = \frac{c}{2}\frac{\nu_2-\nu_1}{\nu_1+\nu_2}$, the probe beam will excite atoms at $v = -\frac{c}{2}\frac{\nu_2-\nu_1}{\nu_1+\nu_2}$. This way the pump beam cannot "take away" atoms from the probe beam and the absorption in the probe beam is more prominent than in the Doppler-broadened case, leaving a dip in the transmission profile.

The blue graphs in Fig. 4.8 show the saturation absorption signal for the D lines in Potassium-39. The frequency scan only shows a small part the whole spectrum. At this point it is important to clarify that the Doppler-free nature emphasizes the transitions and crossover within the Doppler-broadened background, it does not mean that the Doppler-broadening disappears. In Fig. 4.8b, the D2 transition can be identified. The four excited states in the D2 line cannot be resolved and therefore can be

seen as one, leaving us with two transitions and a crossover. Contrary to our previous discussion, one of the transitions seems to exhibit a dip instead of a peak. This dip is caused by the crossover transition for Potassium-41. As our sample is enriched with Potassium-41, its crossover feature is enhanced and covers the transition from the $F = 1$ ground state. We are using the crossover transition of Potassium-39 for locking and therefore the signal from Potassium-41 will not be a problem. As for the D1 line, we are expecting to see nine different features. It can been seen from the plot that only the crossover transitions are distinguishable. This can be understood from the higher signal strength of crossover transitions.

Now that we have a spectroscopy signal, we need to lock the lasers. One can see from the Fig. 4.8, that each feature is symmetric around its extrema. Thus, a feedback loop cannot know whether the frequency of the laser is above or below the reference and therefore, the spectroscopy signal needs to be converted into an lockable signal which is called error signal. Such a signal will be provided by frequency modulation spectroscopy (FM spectroscopy) [90] discussed in the following.

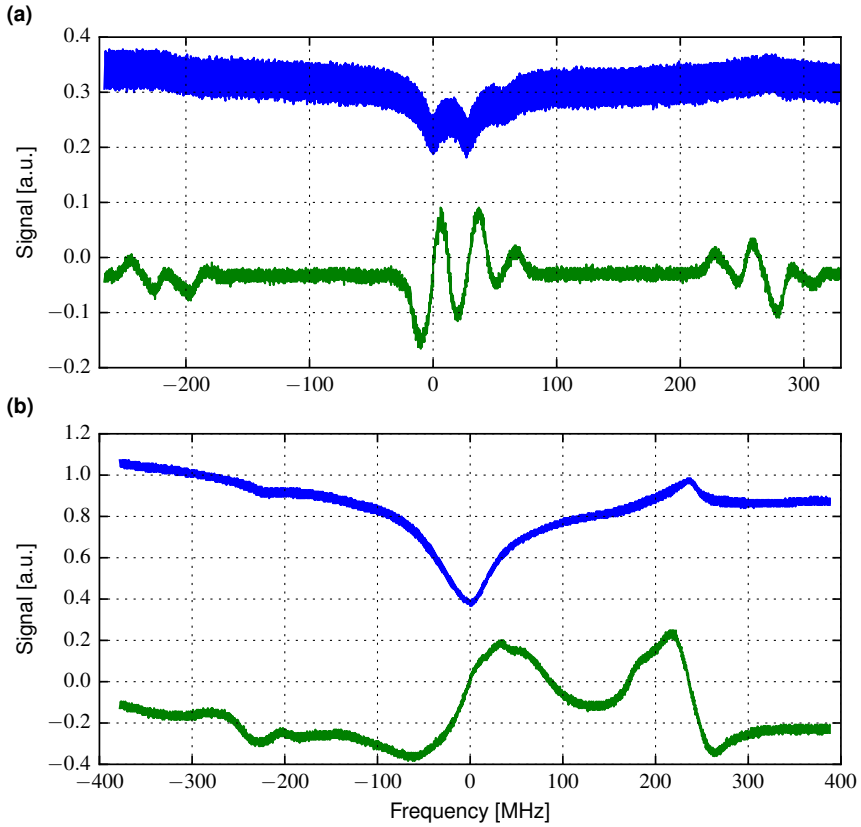

Figure 4.8 – Spectroscopy and error signal for the D lines in Potassium-39. The spectroscopy signal is shown in blue and the error signal from the Lock-In amplifier in green. The peaks represent actual atomic transitions while the dips are crossovers characteristic for this Doppler-free spectroscopy. **a** Spectroscopy on the D1 line. **b** Spectroscopy on the D2 line.

FM Spectroscopy

The general configuration to obtain an FM spectroscopy signal is depicted in Fig. 4.10, the same setup as discussed in 4.2.2. The difference is that the light we sent through the spectroscopy cell is modulated leading to sidebands. FM spectroscopy amplifies changes in the spectroscopy signal while suppressing offsets. The laser field with the additional sidebands is scanned over the transition. The absorption signal is then detected by a photodiode. The signal is post-processed in the electronics by mixing the modulation signal with the signal from the photodiode.

The generation of sidebands at a frequency ω_m is achieved with an electro-optic modulator, in short EOM. The EOM consists of a non-linear crystal where the refractive index inside the crystal can be changed with a voltage, resulting in an electric field on a capacitor around the crystal. By varying the voltage at a frequency ω_m, the effective light field [90] is given by

$$E(t) = E_0 e^{i(\omega_c t + M \cdot \sin(\omega_m t))}, \tag{4.1}$$

where M represents the modulation strength, E_0 is the initial electric field and ω_c represents the carrier frequency of the unmodulated laser. For $M = 0$ the light field is unmodulated. In our discussion, we will consider the scenario of weak modulation $M \ll 1$ [91], allowing us to neglect terms bigger than $O(M)$ and to rewrite the electric field in equation (4.1). Thus, the intensity that will be detected by the photodetector will have the form

$$I(t) = E_0^2 e^{-2\delta_0}[1 + (\delta_{-1} - \delta_1)M \cdot \cos(\omega_m t) + (\phi_1 - \phi_{-1} - 2\phi_0)M \cdot \sin(\omega_m t)]. \tag{4.2}$$

δ_i and ϕ_i signify the absorption and dispersion in the sideband with index i. Another look at equation (4.2) reveals that two relevant contributions are present. The term proportional to $\cos(\omega_m t)$ represents the absorption and the seconds term proportional to $\sin(\omega_m t)$ contains the dispersions. Because the signal from the photodiode is being mixed with the modulation frequency signal, the constant term in equation (4.2) becomes irrelevant. It is important to note that the dispersion and absorption signal depend on the modulation frequency and only differ by a phase of π. This has the consequence that the mixer becomes relevant to convert the AC signal into a DC signal and that by changing the phase at the mixer (or by changing the modulation frequency), we can probe the absorptive or the dispersive part as well as a linear combination of the two. The AC-components that are generated in the mixing process are filtered by a low-pass filter.

Now that we have discussed the generation of the FM signal, we turn towards its specific signal shape. In our discussion, as has been mentioned in the previous paragraph, we will consider only small modulation strengths ($M \ll 1$). The parameter that still is of relevance to our discussion is the modulation frequency ω_m and how it relates to the width Γ the spectral feature. Hereby, we will limit ourselves to the cases where the modulation frequency is much larger than the spectral feature $\omega_m \gg \Gamma$ and

the where the two sizes become comparable $\omega_m \approx \Gamma$. In both cases the absorptive and the dispersive contribution will be discussed.

$\omega_m \gg \Gamma$: In the limit where the modulation frequency is much larger than the feature of interest, the sidebands will independently probe the spectral feature. During the frequency ramp of the carrier frequency ω_c the spectral feature is probed. In the absorptive contribution, the first sideband will reproduce the shape of the saturation absorption signal. Once the second sideband probes the spectral feature, it will do exactly the same. The phase of π between the sidebands causes the second sideband to reproduce the spectral feature with the opposite sign compared to the first sideband (see Fig. 4.9, bottom right). As for the dispersive part, we can again treat the sidebands to be probing the spectral feature separately. This time, the carrier frequency contributes as well (see equation (4.2)). In our limit, we can therefore state that the sidebands and the carrier will see the dispersive change independently. The absorption and dispersion are related through the Kramers-Kronig relations. In the case of a two-level system the absorptive part is Lorentzian. For this discussion it suffices to say that the dispersive term is similar to a derivative of the Lorentzian but the exact form can be found in [92]. It follows that the dispersive FM spectroscopy signal resembles a Pound-Drever-Hall signal (see Fig. 4.9, bottom left).

$\omega_m \approx \Gamma$: In the limit where the modulation frequency is comparable to the width of the spectral feature, we cannot assume that the sidebands probe the spectral line individually. Rather, as the carrier is being scanned over the transition, one sideband will contribute more to the FM signal (namely the sideband at the frequency of more absorption) until the other sideband will dominate. Thus, the absorptive part of the FM signal, like the derivative of the absorption feature, exhibiting the zero-crossing at the extremum (see Fig. 4.9, upper right). Despite the polarity, the FM signal of the dispersive part looks similar to the absorptive part. Intuitively, one can imagine taking the Pound-Drever-Hall signal and squeezing it in the horizontal such that the central feature is more prominent (see Fig. 4.9, upper left).

The parameters we choose for our setup are in the second regime ($\omega_m \approx \Gamma$). In Table 4.4, the properties of the EOMs are listed. One can gather from the table that the center frequencies are comparable to the widths of the spectral feature of interest. The resonance frequency of the EOM for D1 was chosen to be smaller in order to probe the transitions individually (the crossovers for the D1 differ only by a frequency of about 30 MHz).

The FM signal is shown by the green curves in Fig. 4.8. In agreement with the previous discussion, they look like derivatives of the blue absorption spectroscopy curves. While not depicted, a change in the phase will just change the polarity in the FM signal. By changing the phase, it is possible to also tune the zero offset for the FM curves. It is not obvious from our data whether we are probing the absorptive or the dispersive part for FM spectroscopy. A comparison between the upper graphs in Fig. 4.9 tells us that we can determine it from the polarity, the shape and the amplitudes. While the signal of the absorptive part can never exceed $M/2\Gamma$, the dispersive part can. Therefore when changing the phase the maximal signal will be achieved for the

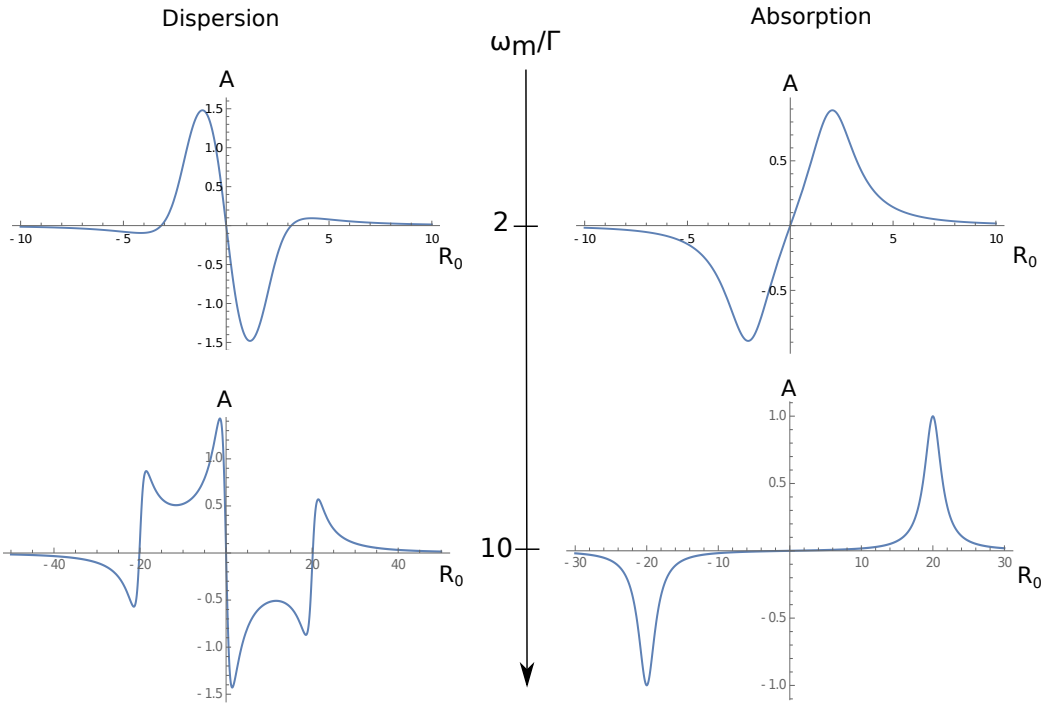

Figure 4.9 – FM spectroscopy for a Lorentzian absorption feature. The left-hand side of the figure contains the FM spectroscopy for the dispersive part and the right-hand side shows the absorptive contribution. In relation to the previous discussion, the cases $\omega_m/\Gamma = 1$ and $\omega_m/\Gamma = 2$ are plotted. The y-axes are normalized by $A = M/2\Gamma$. The x-axes show the scanning range where R_0 denotes the relative position of the carrier frequency with respect to the spectral feature in multiples of Γ the width of the spectral feature.

dispersive FM spectroscopy. From the shape of the two spectroscopies we could also distinguish between the two contributions. Phase fluctuations and noise render it difficult to identify whether the additional extrema in the dispersive curve are present in the data. Lastly, the polarity is the easiest and safest to determine which contribution we are probing. Going back to our graphs in Fig. 4.8 and comparing them to the theoretical plots, we see from the polarity that the dispersive part is probed (note that we are plotting the transmission and not absorption in Fig. 4.8).

EOM	Center frequency [MHz]	Minimal reflection [dB]
MOT-Laser	55.94	-9.96
Image-Laser	53.69	-14.48
GM-Laser	26.59	-8.22

Table 4.4 – EOM properties for FM spectroscopy. The center frequency and the reflection at the center frequency are listed.

FM Electronics

We worked with two electronics setups to generate an FM error signal. The first setup was comprised of separate Mini-Circuit components that were directly connected. This included the essential components such as the VCO (ZOS-50+), Splitter (ZLW-2), Mixer (ZFM-3-S+), Amplifier (ZFL-500HLN+) and low-pass filter (BLP-2.5+). With exception of the amplifier which amplifies the RF signal to the EOM, the build up is represented by Fig. 4.10. In this configuration, the phase was changing by adjusting the cable length between the splitter (or the photodiode) and the mixer. The Mini-Circuit components are inside a housing that shields crosstalk from the high frequency components. Even though this design did work, we decided to go for a Lock-In amplifier on a printed circuit board (PCB).

The Lock-In amplifier was designed by Karsten Förster, the electrical engineer in our group. The implemented features include an LED indicating signal level changes from the photodiode and potentiometers to tune the modulation frequency. With the high frequency shielding in mind, Karsten designed the board to have all low-frequency components on one side of the PCB, separated from all high-frequency components. Many RC and LC filters are implemented to filter the power supply noise or to buffer noise resulting from the board. The advantage of the Lock-In amplifier is the high signal strength compared to our previous solution. This can be accounted to the fact that many amplifiers have been implemented.

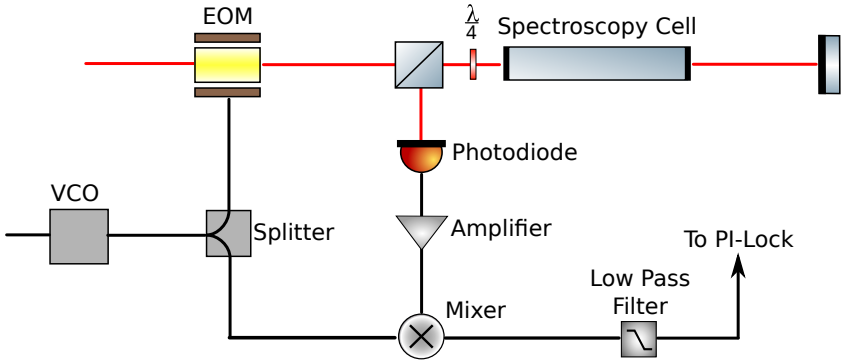

Figure 4.10 – Schematic setup for the saturation absorption spectroscopy and FM spectroscopy. The light from the lasers passes through an EOM where it is modulated. As the polarization is horizontal, the light is transmitted through the PBS, circular polarized by the quarter-waveplate and sent through the spectroscopy cell. Then the beam is retroreflected and sent onto a photodiode. One of the outputs of the photodiode can be used to monitor the spectroscopy signal. The second output is sent into a mixer. The photodiode signal is mixed with the same signal derived from a VCO and sent to the EOM. The frequency is chosen to be the resonance frequency for the EOM and therefore of the sidebands. In the ideal case, the mixer outputs a $2\omega_m$ RF signal and a DC signal where AC contribution is low-pass filtered and the DC contribution is sent to the PI-Lock Box.

Laser Locking

It is possible to lock the frequency of the laser with the error signal and a feedback loop. Laser stability is one prerequisite for any experiment with ultracold atoms. In the time frame of a measurement, frequency drifts and fluctuations need to be minimal. Let us first introduce the feedback loop and identify the parameters that can be influenced. This will give us a general idea for optimizing these parameters. It should be noted that from this discussion, the optimized values will not emerge but instead it will provide a general understanding of the feedback loop. These are determined experimentally. A rigorous optimization of the lock can be done through the phase noise spectral density and a beat between two lasers.

A comparison of the laser linewidth of about 200 kHz for unlocked lasers and the natural linewidth of our desired transitions of 6 MHz tells us that the focus for the cooling laser lies on the stabilization of the long-term frequency changes, namely drifts. Yet, as long as the optimization of the laser linewidth does not compromise the long-term stability, it is our goal to reduce the laser linewidths. This will allow us to use the same locking strategy for the $4S \rightarrow 5P$ transitions in the two-photon Rydberg excitation with a natural linewidth of 150 kHz. While the lineshape of the locked lasers (see Table 4.3) are comparable to the natural linewidths of this transition, this will not suffice. For the two-photon Rydberg excitation, the coherences play an important role demanding the lineshape of the lasers to be as low as possible for the least laser-induced decoherences and in order to increase the lifetime of the Rydberg state[43].

Let us identify the components in our setup with an idealized feedback loop in Fig. 4.11. ν_i is the frequency of our laser. The frequency of the laser can be influenced by a piezo and a DC current modulation, representing the servos. Under the influence of the servo, the frequency is ν_s. The comparison $(\nu_s - \nu_0)$ and the corresponding voltage is realized in the physical setup through FM spectroscopy. Thus, $C(\nu_s - \nu_0)$ can be viewed as the error signal from Fig. 4.8. The voltage is sent to a LockBox PI-Controller whose output is translated into a voltage on the piezo and a current on the laser diode. This is denoted by the $(D \cdot g(f))$-term. In order to know the general form of $g(f)$, the specifics of the LockBox PI-Controller need to be clarified.

The PI-Controller has been designed in-house. In essence, the circuit for the LockBox is a PI-Loop with a second integrator. The first PI-Loop is for the current servo. The PI-Loop in combination with the second integrator gives the piezo servo. Introducing an additional integrator also introduces a second timescale to the feedback loop. Double integration leads to higher gains on low frequency scales reducing drifts. Figure 4.12 shows the frequency dependent servo gain and the phase. The gain and phase for the current servo are shown in red while the piezo servo is depicted in blue. While important for the lock characterization, the vertical scale is not given since the LockBox has not been characterized in the thesis. For the servo gain, it is possible to observe that the integrator acts as low-pass filters and has 20 dB loss per decade. An integrator causes a phase shift of $\pi/2$ which tends towards zero as the

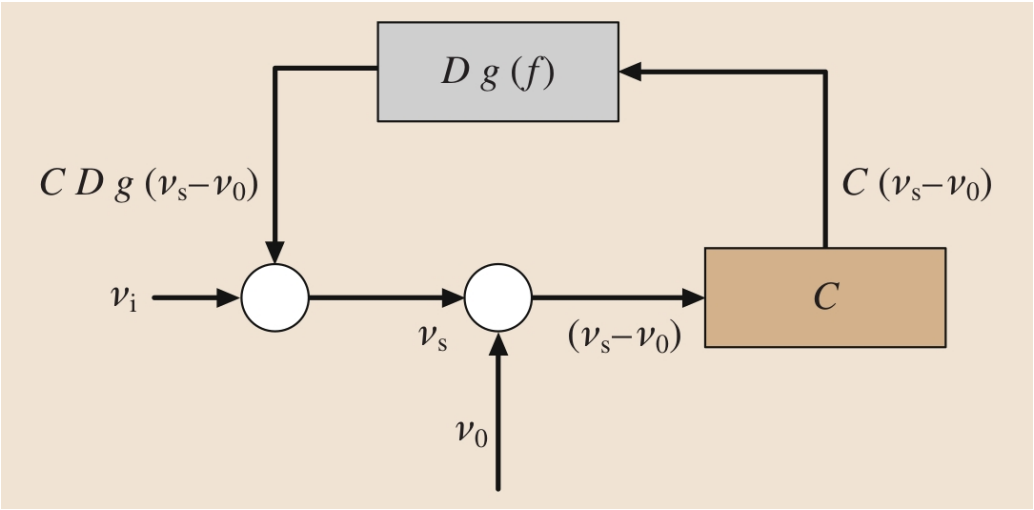

Figure 4.11 – General feedback loop for laser locking. ν_i represents the initial frequency of the laser. ν_s is the frequency of the laser as corrected by the servo loop. ν_0, the center frequency, and ν_s are compared, where the difference between them translates into a value $C(\nu_s - \nu_0)$. The value is then amplified by the servo amplifier where $g(f)$ is the frequency dependent gain and D represents how the voltage translates back into the action of the servo. The resulting signal is acting as the new servo signal to correct the initial frequency. Adapted from [93].

gain of the integrator becomes negligible. In the case of the piezo servo, a region of 40 dB loss per decade is present by the double integration. With the second integrator, there is no frequency-independent gain. The characteristic timescales are indicated by f_p and f_{di}. These frequencies result from the transfer function of the integrators and the amplifiers. The servo gain is given by the absolute value of the transfer function and the phase is given by the argument of the transfer function. We can observe the phase of 90° caused by the integrator for the PI-Loop and the phase shift of 180° for the double integrator. We can now turn to the parameters that we can tune to optimize the feedback loop:

- Input gain: The input gain can be controlled with a potentiometer. Going back to our feedback loop in Fig. 4.11, this influences the amplification of the term $C(\nu_s - \nu_0)$ and therefore an amplification of the error signal.

- Proportional gain: This potentiometer will increase the level of the proportional gain and therefore shift f_p to lower frequencies .

- Slow integrator: A potentiometer that influences f_{di}. For a higher resistance f_{di} is decreased.

- Fast integrator: Just like the slow integrator, the frequency f_p can be influenced by changing the resistance. Note that this parameter influences both servo branches.

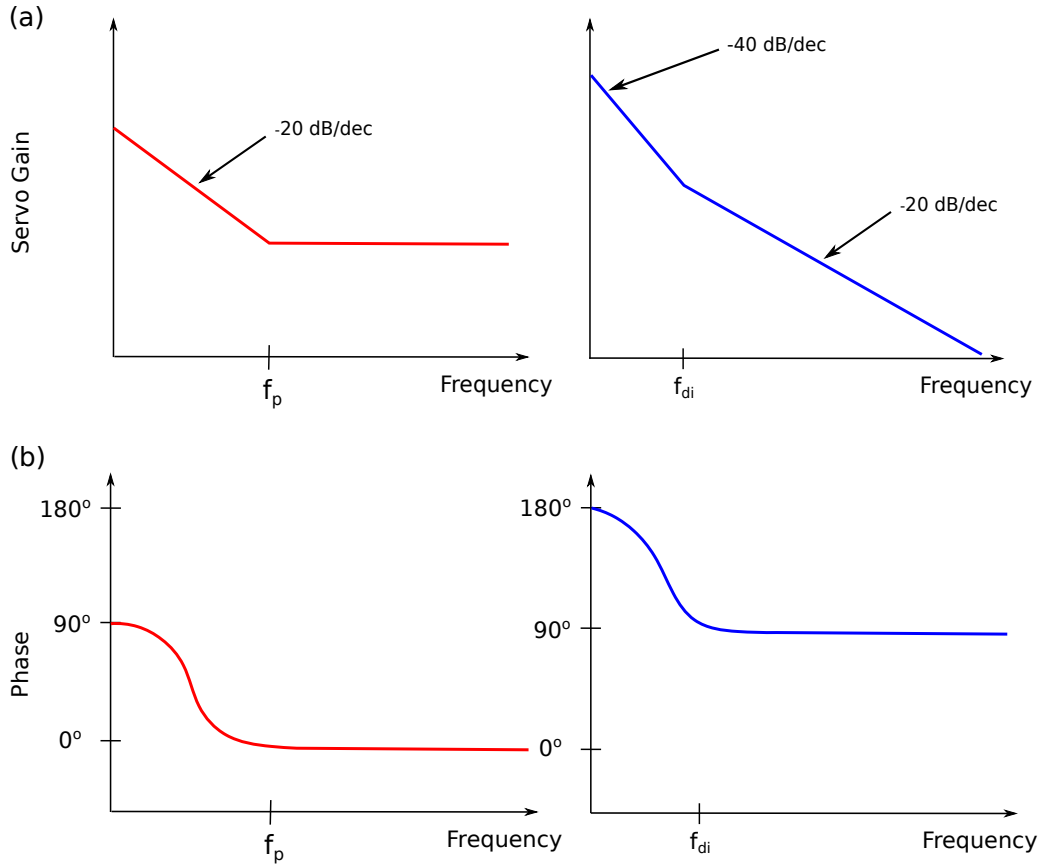

Figure 4.12 – Bode plot for servo gain and phase. A Bode plot for the gain is given by a log-log plot while the Bode plot for the phase is a lin-log plot. a The servo gain for the piezo (blue) and the current (red) servo are sketched. Note that this is a linearized Bode plot. **b** Sketch of the phase for the piezo and current servo. An integrator causes a phase shift of $\pi/2$.

- Input inversion: The sign of the input signal can be changed through a jumper. The sign takes effect on the fast and the slow output.
- Slow inversion: The sign of the piezo servo can be changed through a jumper. The sign change only affects the slow output and therefore the piezo.

We can now discuss the general procedure for the laser locking. For the long term stability, we want to make sure that the gain at low frequencies is as high as possible and the reason we implemented the double integrator for the piezo in the first place. Second, in order to influence the changes on the short timescales, we need to ensure a high gain on the high frequency scale. There is a limit to the gain that we can apply to the system since resonances lead to an instable feedback loop. This can for example lead to a jittering laser and thus even a larger laser linewidth than for an unlocked laser.

Ensure negative feedback - The first step for laser locking is to ensure that the feedback is negative, in essence, countering the laser frequency change towards the de-

sired frequency. In order to do so, it will be useful to reduce the gains as resonances will hardly allow us to see the polarity of the feedback loop. Input inversion and slow inversion are the parameters that need to be changed. First, it will be useful to only operate the piezo and disconnect the current modulation. As one attempts to lock the laser, one should observe the error signal approaching zero voltage. If this is not the case, either the gain on the piezo is incorrect or the feedback is not negative. Once the error signal keeps a zero voltage during the lock, it is possible to change the polarity of the fast output. Again, for non-exaggerated parameters, one should observe again how the error signal goes towards zero. If the piezo and the current have opposite polarities, the error signal will not remain zero for a considerable time since the both servos counter each other. Changing the jumpers on the input inversion and the slow inversion simultaneously will lead to the correct polarity on both servos.

Gain and characteristic frequency of the piezo servo - Once the polarity is set, one can tune the gain on the PI-Loop for the piezo. Influencing the proportional gain and slow integrator allows for a shift in f_{di} and the low-frequency gain. The piezo servo output can be observed on a frequency analyzer. A disturbance on the laser will result in a servo bump. A servo bump indicates that we the servo works against a disturbance. Besides the servo bump (not a resonance), no other features should be pronounced, otherwise the gain needs to be reduced.

Gain and characteristic frequency of the current servo - The current servo, important on the short timescales, will be influenced by the fast integrator,slow integrator and the proportional gain. A higher proportional gain and slow integrator decreases f_{di}. Since the two servos are not independent from each other, one needs to be aware that a changes on the current servo will influence the piezo servo. The most practical way at this point is to tune the parameters and to iteratively measure the feeback response of the slow and fast output. Servo bump should be present around the characteristic frequencies for the two servo branches.

Overall gain - The overall gain can be changed with input gain. This parameter is especially useful if one does not want to change the frequency dependent gain $g(f)$ but just increase the gain due to small changes in the system, like a weaker or stronger error signal caused by a frequency change on the EOM.

4.2.3 Tapered Amplifier

In order to supply enough laser power for the MOT and for the grey molasses, the light from the laser must be amplified. An inexpensive and efficient way to amplify a lasers in range of $650 - 1000\,nm$ is to use optical amplifiers such as tapered amplifiers (TAs). The active region of a tampered amplifier is a semiconductor (e.g. GaAs). By applying a injection current to the TA, electrons are being pumped from the valence band to the conduction band. Without any laser input spontaneous decay will

cause the tapered amplifier to fluorescence while in the presence of the laser beam, the conversion from the conduction band to the valence band happens in a stimulated fashion.

TA Chip and Design

In optical setup we are using two tapered amplifiers. One is for the MOT-Laser (767 nm) and the other for the D1 laser (770 nm). Both TAs contain the same TA chip (Eagleyard EYP-TPA-0765-01500-3006-CMT03-0000) where the gain region of the medium is trapez-shaped and allows for more output power.

Seed Power	Center Wavelength	Aperture	Divergence Angle	Temperature	Max. Current
P_{seed}	λ_c	d_{input}/d_{output}	$\Theta_{\|\|}$ / $\Theta_{\perp}$	T	I_{max}
10 - 50 mW	765 nm	3 µm - 190 µm	14 ° / 33 °	5 - 40 °C	3.3 A

Table 4.5 – Basic specifications for the TA chip.

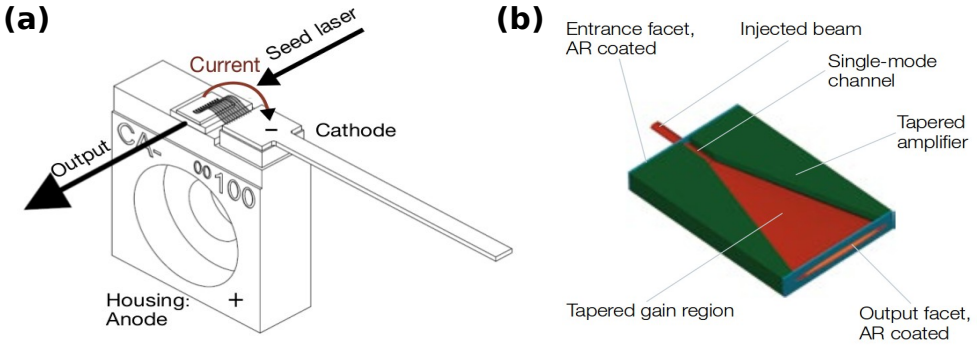

Figure 4.13 – TA mount and chip. a The TA mount depicted from the output direction. The TA chip is indicated by the position of the wires. The current passes from the anode through the TA chip onto the cathode. The current supplies the electrons to participate in the stimulated emission when a seeding laser is present. **b** A trapez-shaped TA chip. The red part depicts the active region. The seed laser is being injected from the entrance facet, amplified in the active region and emitted from the output facet.

The TA chip is mounted to a copper block with good heat contact. This copper block is being cooled by two Peltier elements (Adaptive ETH-071-14-15-RS) which again are surrounded by two water cooled copper blocks as can be seen in Fig. 4.14. As the temperature plays a crucial role in the output power of the TA chip, efficient cooling for the TA chip is necessary. Heat paste was applied to improve the heat conduction between the Peltier elements and the copper blocks. The purpose of the water cooled copper blocks is to carry away heat that would otherwise feed back into the system and would not allow proper operation for longer times. The TA chip and its copper mount are fixed onto a 30 mm cage system together with two translation mounts (Thorlabs SM1Z) that move aspheric lenses (Thorlabs C230TMD-B) with a

focal length of f = 4.51 mm. The first lens focuses the incoming beam onto the active area of the tapered amplifier. The second lens is for the collimation of the outgoing beam. The cage system is fixed onto a mount of aluminium. High and stable output powers for the TA require the components in the cage system not to move relative to each other once the seeding has been optimized. The aluminium mount and the cage system support the water cooled copper and thus the TA chip. To protect the system against external influences, the sides and the lid of the TA are made from acrylic glass. This prevents dust settling on the delicate TA chip or the lenses. Furthermore, it reduces air fluctuations.

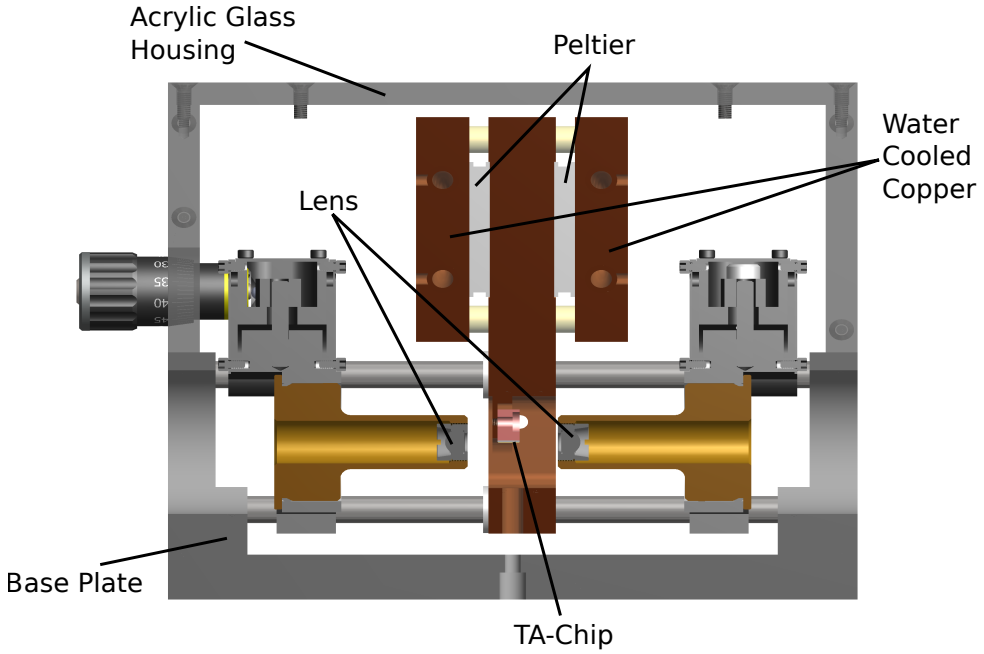

Figure 4.14 – Tapered amplifier design. The TA chip is fixed to a copper block. This copper block is cooled by two Peltier elements. The hot side of the Peltier elements is in contact with two copper blocks which are water cooled. The mount of the TA chip and two translation mounts are placed onto a 30 mm cage system. This cage system is fixed onto an aluminium mount. The cover is made of acrylic glass.

Optimization of Output Power

In consideration of all the losses before the beams enter the vacuum chamber, the output of the TA should be 1.5 W. For fixed seeding powers and TA-current, the optimization of the amplification can be achieved by the incident parameters of the beam (beam size and shape, polarization) and the temperature of the TA chip. Once the lenses and the beam profile are determined, the incident parameters can be adjusted by beamwalking. The position of the beam as well as the angle with which the beam hits the lens and gets focused onto the chip are important. After that, one can change the temperature of the TA chip and with it the efficiency for the amplification. As

can be seen in Fig. 4.15, a temperature range of 15°C has been scanned. The optimal temperature for the TA amplifying the MOT-Laser was at about 19.5°C. For the TA that amplifies the GM-Laser the power seems to be better, the colder it the TA chip gets. Despite the small efficiency gain, the temperature should not be reduced below 19°C for long-term operation in order to avoid the possibility of condensation.

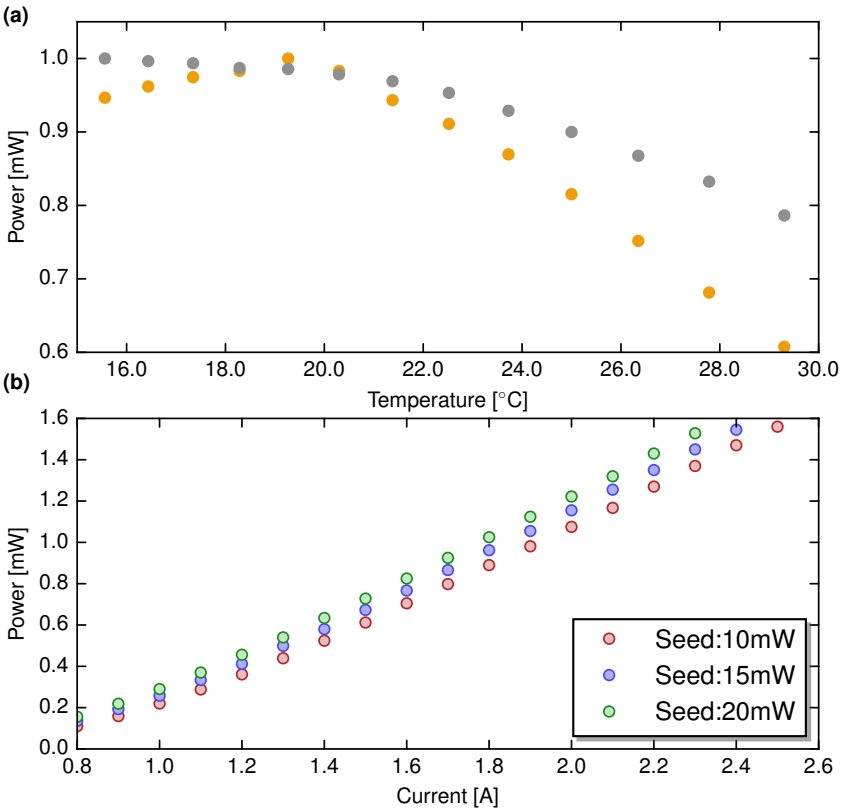

Figure 4.15 – Optimizing the output power of the tapered amplifier. **a** The output power of the TA can be influenced by changing its temperature. The measurement was taken for the TA of the MOT-Laser (in orange) and the TA of the GM-Laser (in grey). **b** The output power of the TA is shown for three different input powers of 10 mW, 15 mW and 20 mW. To stay in accordance to the optimal operational parameters of the TA chip the output power of 1600 mW was not exceeded. The large influence of the current and the small influence of the seeding power indicates the efficient amplification.

To characterize the performance of out TA chip as to its amplification and saturation, we measured the output power as a function of the current for three different seeding powers (10 mW, 15 mW, 20 mW). The power was measured with a powermeter (Thorlabs PM100D, sensor: Thorlabs S314C). Figure 4.15 shows a strong dependence of the output power of the TA on the current and a weak impact of the seeding power on the output. The weak dependence on the seeding power tells us that we are operating the chip at saturation and the strong current dependence indicates that more electrons need to participate in the stimulated decay from the conduction band into the valence band.

Optimization of Beam Shape

The problem with tapered amplifiers, especially the trapez-shaped tapered amplifiers is the output beam shape. The asymmetric shape of the active region's rear side inhibits the collimation of the beam with only one lens. Therefore the aspheric lens (Thorlabs C230TMD-B) can be used to collimate one direction and reduce the divergence in the other direction. By additionally using a cylindrical lens the other direction can be collimated. The focal length of the cylindrical lens is chosen such that the beam is as close to spherical. In our case we used a cylindrical lens with a focal length of 75 mm. From the comparatively big focal length one can deduce that the beam sizes were also large. For the quick operation of the AOMs, we can accept beam diameters below 1 mm. Therefore, we placed a 2:1 telescope and a 3:1 telescope after the TA for the MOT-Laser and for the TA after the GM-Laser respectively. The reason we used two different telescopes is that initially we intended to use AOMs for the grey molasses beams that have a smaller aperture than for the MOT-beams. Although this is not the case, we remained with the telescope with the benefit of a smaller beam.

4.2.4 AOM Paths, Recombination and Fiber Coupling

This subsection describes the last part before sending the beams to the experimental table. After amplifying the MOT-Laser and the GM-Laser to 1.5 Watts of power each, we derive MOT_C, MOT_R, $Zeeman$, GM_C and GM_R. All beams undergo an AOM double pass. The cooler and repumper beams for the grey molasses and the MOT are then recombined before being sent into the fiber. The beams for imaging and the Zeeman slower are coupled into the fibers without recombination.

AOM Paths and Shutters

The laser system for cooling, trapping and imaging potassium relies on many different frequencies. In total, eight beams need to be controlled individually. Either because the detunings are different or in the case of the imaging beams because we want to be able to image the MOT cloud from different directions independently. With the lasers being locked on the crossover transition, we can reach all necessary frequencies with commercial AOMs. The crossover does not resemble a physical transition which in turn means that all of our beams need to be detuned. Table 4.6 summarizes all different single pass detunings for the first attempts to get a MOT signal. These values are based on considerations that will be discussed in sections 4.4 and 4.5.

All our AOMs (Gooch and Housego AOMO 3100-120) have a center frequency of 110 MHz and are mounted onto a rotation mount (Misumi RTSS60) with no electrical contact to the stage. The AOM is placed at the center of the rotation mount such that we can turn the AOM without considerably displacing the aperture. We supply our AOMs with RF power that originates from in-house AOM-Drivers and is attenuated before reaching the AOM. The attenuator reduces the reflected power from the AOM which can damage the driver and is needed for the proper operation of the AOMs. The single pass diffraction is optimized when the RF power is modulated at a single

Beam	GM_R	GM_C	MOT_C	MOT_R	Image	Zeeman
Single Pass Frequency [MHz]	124	−106	−116	115	−107	−197
Double Pass Efficiency [%]	72.1	80.5	72.0	71.5	70.5	n/a

Table 4.6 – AOM single pass detuning and double pass efficiency. Detunings and efficiencies for the AOM retroreflectors. The first row shows the single pass frequencies of the AOM. The second row shows the double pass efficiency. The efficiency for Zeeman is not given because the AOM was changed and no measurement is available. Similar values as for the other AOM paths are expected.

frequency. Our AOM-Drivers output also at higher orders when operated at powers below 1.5 Watts. Since the AOMs need an RF power of approximately 1 Watt, depending on the single pass frequency, we attenuate the driver's output of 1.6 Watts with a 2 dB attenuator.

As part of the AOM characterization, we measured the switching times of our AOMs. For the imaging of our atoms, fast switching times are essential. Even though the MOT cloud will be illuminated for several microseconds (between 5 to 20 µs), we want to assume that illumination pulse has a constant power. A rough estimate can be made by dividing the beam diameter by the speed of sound in the crystal of the AOM. Assuming a beam diameter of about 1 mm and an acoustic velocity of 4.2 mm/µs, the rise time τ_{rise} can be determined to be 240 ns. This would be short enough not to consider the pulse shape when turning on the AOM. For the measurement, we define the time between 10% to 90% maximal power to be the rise time. The measurement has been performed by sending a TTL signal to switch the AOM-Drivers and measuring the power after the AOM double pass. From the data we can also infer the delay τ_{delay}. The delay is defined as the time between the switch of the TTL signal to 10% of the maximal power. In Table 4.7, we can see that the rise times are below the estimated rise times and far below the time of the image pulse.

AOM	MOT_C	GM_C	Image
Delay τ_{delay} [ns]	370	570	450
Rise Time τ_{rise} [ns]	130	150	160

Table 4.7 – AOM delay and rise times. The measurement was taken for one beam for the grey molasses, one for the MOT and one for the imaging. Since the rise time is a function of the beam size, we expect to have similar results for the repumping beams.

We operate our AOMs in a double pass configuration. A double pass configuration can simply be achieved with a mirror sending the light back through the AOM causing the light to deflect twice and thus picking up twice the detuning. The problem with a single pass is that the diffraction efficiency, not to mention the fiber coupling efficiency, will suffer greatly from the frequency dependent diffraction angle. Therefore we resort to a cat's eye configuration. The main advantage is that frequency-dependent steering effects can be reduced due to an 4f imaging. A detailed descrip-

tion for the cat's eye retroreflector can be found in [94].

We quantify the tunability or effective linewidth of the AOM cat's eye configuration by measuring the double pass diffraction and the fiber coupling efficiency for different RF frequencies. In preparation of the measurement, we need to optimize the efficiencies for single pass detuning in Table 4.6. The diffraction efficiency was measured with a power meter after an iris that blocks the unwanted orders and the coupling efficiency was measured after the fiber outcoupler. We expect that the diffraction efficiency decreases when deviating from the center frequency whereas the fiber coupling should remain unchanged if the lens is placed correctly for the 4f imaging. Figure 4.16 shows the double pass efficiency and the fiber coupling efficiency for four different AOMs. GM_R and MOT_C meet our expectations. For the other beams, we see different results due to a combination of non-perfect fiber coupling and 4f imaging. This is not necessarily a bad thing and could even be used to increase the AOM tuning range. One can even attempt to optimize the fiber coupling for an RF frequency to the frequency that gives the best double pass efficiency and therefore increase the tunability. From the data points, we can extract the linewidth which in this case is defined to be the full width at 0.85 of the maximum. The value of 0.85 is not arbitrary but gives a conservative estimate on the power losses we can tolerate for the MOT or grey molasses. From the fit we can extract that we have a tunability of about 2Γ for the double pass around the center frequency. Having such tunabilities helps to minimize temperatures and maximize phase space densities without physically adjusting the setup. Moreover, tuning the AOMs as part of the cooling scheme can be useful as discussed in section 4.5.

Besides the detuning of laser beams AOMs can also act as switches. In the case of the image laser, it is not enough to use the AOM for switching. Depending on the axis we want to image, we need to be able to block two out of three image beams. Since all the image beams are derived from the same AOM, we implemented mechanical shutters into our setup. They allow us to individually gate beams and ensure that our atoms in the vacuum chamber are not exposed to stray light from the AOM paths. To reduce stray light, we placed shutters for the beams. The design of the mechanical shutters consists a front plate with a 3 mm aperture and a thin aluminium sheet attached to a speaker. Due to the front plate, the shutters can only be placed once the AOM paths have been optimized. Initialized by a TTL signal, the speaker lifts the aluminium sheet into the beam path. To reduce vibrational effects on the surrounding optics from the mechanical shutting, we fixed the shutters onto sorbothane sheets. For the control of the experiment it will be interesting to quantify the jitter, delay and rise time of the shutters. Jitter refers to variation for delay and rise times at different instances.

The shutters are switched with a frequency generator connected to a TTL input. At an increment of 5 µs, we could not observe jittering on the oscilloscope. Without further investigations we therefore measured the delay and rise times from a measurement such as depicted in Fig. 4.17. The figure shows the normalized power over

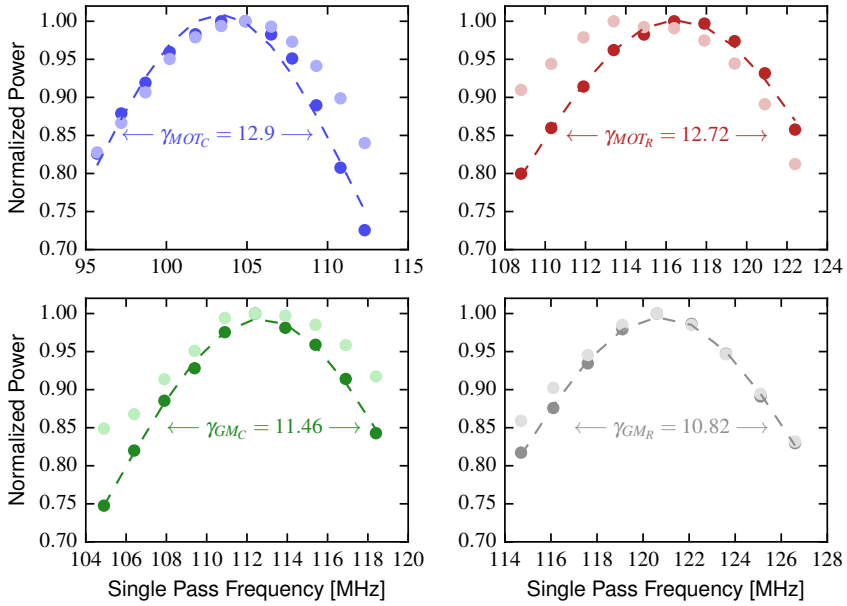

Figure 4.16 – AOM double pass and fiber coupling efficiency. The light points indicate the efficiency of the double pass in the AOM while the dark points show the fiber coupling efficiency. From the dark spots we can extract the bandwidth of our double pass configuration. The dashed lines serve as a guides to the eye. Note that the center frequencies are different than noted in Table 4.6 due to adjustment of the AOM detunings after the measurement has been performed. Difference in the bandwidth are not expected.

time. Initially, the shutter is blocking the beam. After the TTL signal switches, the shutter opens and the beam can reach the photodetector. The delay t_{delay} is defined to be the time that the TTL signal is below 2 Volts (the shutter closes when the TTL signal is shut off) to the time that 10% of the normalized power are measured. Using a definition of rise time t_{rise} as the time elapsing between 20% to 80% of the normalized power, we obtain the results summarized in Table 4.8. One can see that for GM_C the result is very different than for the other shutters. We do not have a consistent explanation for this and therefore we consider it to be an artifact of this shutter. As the rise times depend on the beam diameter, the results are comparable.

AOM Path	GM_R	GM_C	MOT_C	MOT_R
Delay t_{delay} [ms]	1.80	1.07	1.70	1.72
Rise Time t_{rise} [ms]	0.10	0.13	0.09	0.06

Table 4.8 – Shutter delay and rise times. This table summarizes the delay and rise times for four shutters in our optical setup. With the exception of GM_C, the delays of the shutters are similar. The rise times for all the different beams are comparable.

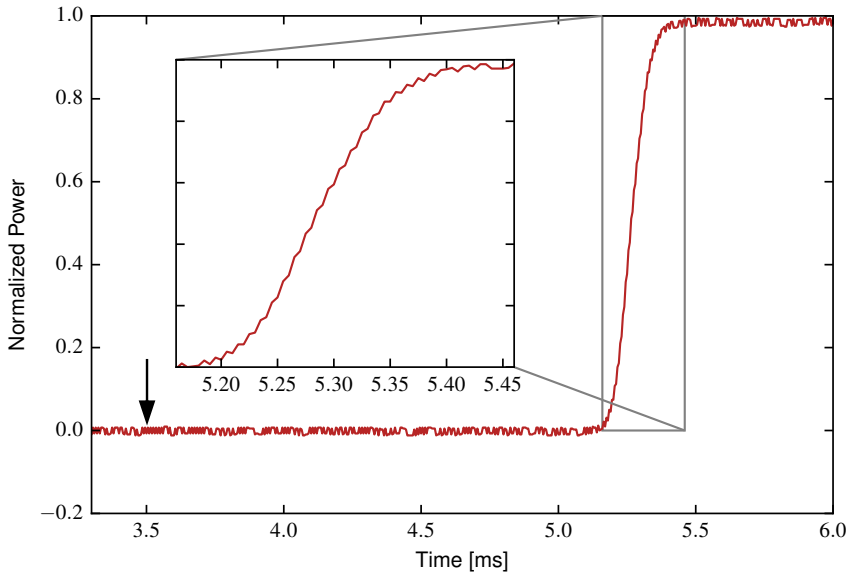

Figure 4.17 – Laser power for an opening shutter. The figure shows the normalized laser power after the fiber for a typical AOM path, in this case MOT_C. The black arrow indicates the time that the TTL voltage dropped below 2 Volts. From this curve, one can estimate the delay time of the shutter. The rise time can be taken from the inset. The fluctuations can not be traced back to noise but rather to the resolution limit of the oscilloscope.

Recombination and Fiber Coupling

The cooler and repumper for both the MOT and the grey molasses are recombined and coupled into three different fibers, corresponding to the three perpendicular directions.

Our initial idea was to use an interference filter for the recombination, the same one used in our linear lasers which transmits 767 nm and reflects 770 nm light. The setup would therefore be more compact than the recombination depicted in Fig. 4.3. In order to realize such a recombination, one needs to combine the 770 nm beams and the 767 nm beams, optimize the fiber coupling for 767 nm, insert the interference filter and optimize the fiber coupling for 770 nm. After a first test, we decided against this. The reason is simply that the sensitivity of the interference filter on angle of the incoming beam was too high. We were essentially not limited by the fiber coupling efficiency but by the power losses that we experienced from the interference filter. Although it seems to be a simple solution, it was deemed impractical for our setup.

We decided to use a more conventional way of recombining. At the expense of inevitably losing 25% of the power, we recombined the beams as depicted in Fig. 4.3. The long distances that the beams travel compared to the previous method led to the conclusion that fiber couplers should be placed to have similar beam paths. With many waveplates and polarizing beams splitters, it is not surprising that the power distribution between the different fibers is not uniform. The coupling efficiencies and

the power distributions are summarized in Table 4.9. We have measured the power in front and after the fiber with a powermeter to determine the efficiency.

	Rec. 1	Rec. 2	Rec. 3	Rec. 4	Image (Im1)	Zeeman
GM_R in GM_R eff.	52.9 mW 65.2 %	68.7 mW 60.6 %	53.5 mW 49.5 %	68.5 mW 59.4 %		
GM_C in GM_C eff.	77.0 mW 62.9 %	59.1 mW 57.7 %	61.0 mW 46.7 %	79.6 mW 56.6 %		
MOT_R in MOT_R eff.	58.2 mW 51.0 %	58.2 mW 51.8 %	69.5 mW 41.0 %	51.5 mW 52.6 %		
MOT_C in MOT_C eff.	88.0 mW 51.8 %	88.3 mW 51.7 %	90.1 mW 48.1 %	86.2 mW 50.2 %		
Zeeman in Zeeman eff.						12.33 mW 60.0 %
Image in Image eff.					6.44 mW 75.6 %	

Table 4.9 – Fiber coupling efficiencies. Power insertion and fiber coupling efficiencies for Doppler and sub-Doppler cooling. Empty cells indicate that the beam is not send into that fiber. In the case of the image beam the splitting into the three spatial directions happens very close to the fibers. Therefore, the values are not shown for all the fibers.

4.3 The Experimental Apparatus

In this section, we will discuss the heart of the experiment, the vacuum system. In 4.3.1, we will cover the general vacuum system, this includes all the essential parts connected to the vacuum system starting at the atomic oven up to the ion pumps. In 4.3.2, we will take a closer look at the vacuum chamber and the components that were implemented into the vacuum chamber. The design will be presented, motivated and, where instructive, the functionality for a quantum many-body experiment with Rydberg atoms will be elaborated.

4.3.1 General Vacuum System

Ultra-high vacuum is a prerequisite for experiments with ultracold atoms. A low pressure of the background gas will increase the lifetime of our atoms and reduce the coupling of our quantum simulator with the environment. For our vacuum setup, we are aiming at pressures below 10^{-11} mbar. Yet, we require a high flux of potassium atoms for low cycle times. In Fig. 4.18, a render of the vacuum system is depicted. In the following, we will discuss each of the labeled parts whereas the Zeeman slower will be excluded from this discussion and treated extensively in section 4.4.

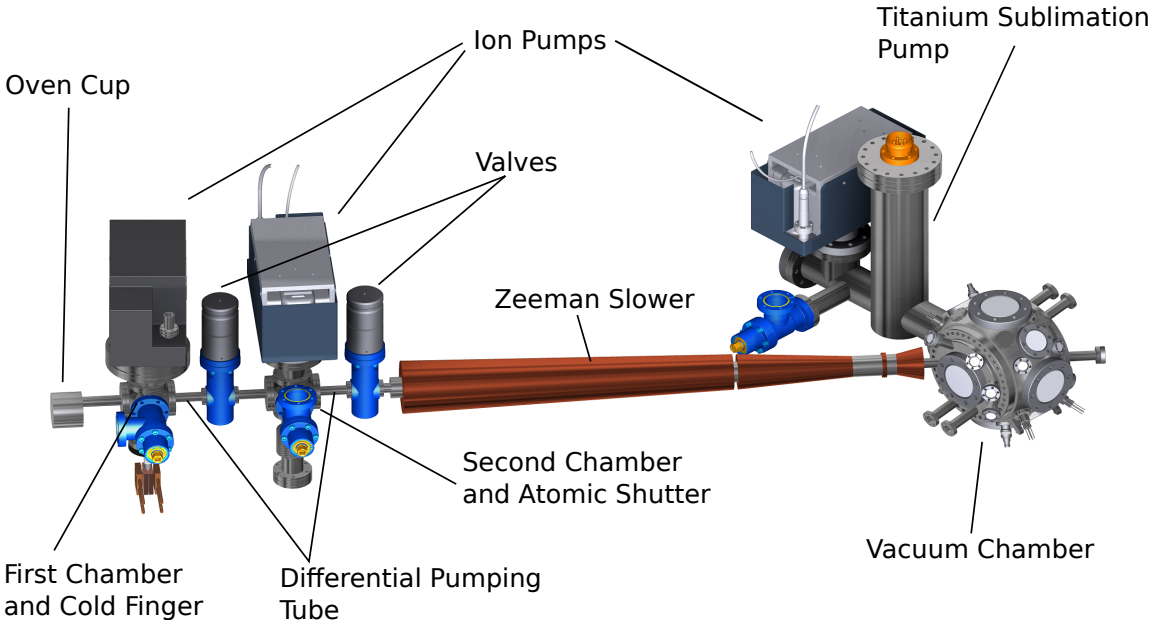

Figure 4.18 – Render of the vacuum system. This render depicts the vacuum system of our experiment with the most important parts being labeled. Some of the labels refer to parts inside the vacuum system and therefore not visible in the render. For reason of simplicity, not all the details of the vacuum system are depicted such as the high voltage on the vacuum chamber.

Atomic Oven A high flux and collimated beam of atoms for quick loading times is provided by an atomic oven. The atomic oven consists of three parts: an oven cup, seen in Fig. 4.18, a nozzle and a heating element. Potassium can be inserted into the oven cup before screwing on the nozzle which has an aperture of 3 mm for collimation. The nozzle opens up towards the oven cup and allows potassium to flow back into the oven cup. The heater can be clamped externally where temperatures of 160 °C have been reached in preliminary tests. This is considerably more than the temperatures we are planning to use for Potassium-39 of around 100 °C leading to atomic vapor pressures of about 10^{-5} mbar. The heater was purposefully designed for higher temperatures if we work with the Potassium-40 isotope.

First Chamber and Cold Finger After the atoms leave the nozzle of the oven, they enter the first chamber which contains a cold finger and is pumped by an ion pump. The cold finger is made of two copper sheets with an aperture of 3 mm placed at the height of the atomic beam. The copper sheets are connected to a high-current feedthrough which is cooled to −20 °C by two Peltier elements. The Peltier elements are connected to the high-current feedthrough on the outside of the vacuum. The cold finger serves the purpose to further collimate the atomic beam and to reduce the temperature of the potassium sticking to the cold finger and thus its vapor pressure. From the experience of other groups, we know that potassium reacts aggressively with metals and reduces the life time of the ion pumps. The reduced pressure, dropping three

orders of magnitude at $-20\,^{\circ}\mathrm{C}$, will increase the lifetime of the ion pumps. The collimation of the cold finger reduces the amount of potassium reaching gaskets and causing leaks. As additional measure, most of the connections in the first chamber are made with nickel instead of copper gaskets.

Second chamber and Atomic Shutter The collimated atom beam passes through a differential pumping stage and a valve before reaching the second chamber. Besides the second ion pump, the chamber houses the atomic shutter. The atomic shutter is very important for the experimental sequence. We want to be able to stop the flow of (hot) potassium atoms reaching the vacuum chamber e.g. after the cooling stages or while we are performing an experiment in the optical lattices. The atomic shutter is made of a shutter stick screwed to a bendable bellow. A pneumatic piston (Festo ADN-32-10-A-PPS-A) will push the bellow creating a tilting motion that will displace the shutter stick and therefore the atomic beam can pass through the Zeeman slower. Once the piston returns to its relaxed motion, the shutter stick blocks potassium from reaching the Zeeman slower.

Differential Pumping Tubes A way to combine high flux of potassium with a ultra-high vacuum (UHV) setup is through the use of differential pumping. Differential pumping favors a collimated atomic beam over the background gas. While a collimated beam ideally passes through the differential pumping area without any collisions on the walls, the uncollimated background gas will undergo many collisions with the tube and the other molecules. This leads to a much lower conductance of the background gas. According to [95], the conductance of air at room temperature in liters per second is given by $12.2 \cdot d^3/l$, where d is the diameter of the tube and l is the length of the tube. This value is only true in the free molecular regime ($< 10^{-6}\,\mathrm{mbar}$ [96]). Our tubes with a length $l = 70\,\mathrm{mm}$ a diameter $d = 3\,\mathrm{mm}$ will yield a conductance of about $5 \cdot 10^{-3}$ liters per second. The ratio of the conductance and the nominal pumping speed of air being $55\,l/s$ will give us a differential pumping ratio of $0.85 \cdot 10^{-3}$.

Valves We have implemented two valves into our setup. The idea of the valves is to isolate different parts in the vacuum system. It is important that if a leak occurs that we can work on the leak without disturbing the rest of the setup. The first stainless steel valve (VAT 48124-CE01-0001) is placed after the first differential pumping stage. The second valve (VAT 48124-CE44-0001) is placed immediately before the Zeeman slower. The location of the valves has been chosen on the basis that works on the vacuum system will likely occur in the first two chambers. We might have to replace the potassium at some point and there is also a risk for the cold finger to become clotted. As mentioned before, the vapor pressure in the first chamber might cause the ion pump to break and also leaks due to remnants of potassium on the vacuum connections can occur.

Vacuum Pumps Three vacuum pumps are constantly connected to the vacuum system. These are ion pumps that are employed after the bake out. They maintain the desired pressure in the vacuum chamber. The first pump (Varian VIP 75 l/s Ion Pump) is connected to the first chamber. A chevron buffle was placed between the first chamber and the ion pump to reduce direct access for the potassium atoms and increase the lifetime of the ion pump. For the second chamber and the vacuum chamber we use the same type of pump (Agilent Vacion Plus 55 Starcell).

Titanium Sublimation Pump Titanium sublimation pumps (TSPs) help us to reduce the pressure for UHV vacuum. By applying high currents through the titanium filament, the titanium sublimes (transitions from a solid to the vapor phase) and gets deposited on the walls. In contrast to ion pumps, inert gases e.g. Helium and Argon are not pumped out to reduce the pressure but instead, react with the titanium and solidify on the walls of the titanium chamber. The location for the titanium filament has been selected to prevent direct field of view to the vacuum chamber and therefore reduce titanium contamination.

4.3.2 Vacuum Chamber

The spherical square vacuum chamber (Kimball MCF800-SphSq-G2E4C4A16) is made of one stainless steel part. The vacuum chamber contains an in-vacuum objective, electrodes, an ion detector, vacuum coils and RF antennas. Flanges for the vacuum chamber have been produced by our workshop such that the vacuum coils or the ion detector can be mounted inside. A render of the vacuum chamber can be seen in Fig. 4.19. The objective and the electrodes are connected to the flanges with groove grabbers, allowing for precise and flexible mounting. On the two CF 160 connections, we placed custom flanges. The flanges have multiple viewports, one CF 16 connection for the Zeeman slower and the vacuum coils are soldered to them. The chamber with the titanium sublimation pump and ion pump are connected through a CF 63 flange. The bigger viewports (CF 40, CF 63) have a broadband antireflection (AR) coating. The CF 16 viewports on the other hand are AR coated for lattices at 532 nm and 1064 nm. It was important for the design of the vacuum chamber and the components that are inside to have enough optical access for the present optics setups and with foresight to future addition.

Objective Our objective was produced by Special Optics and is built into the vacuum chamber. The objective is composed of a lens triplet with a hole in the middle. The hole with an aperture of 8 mm allows us to send beams in the vertical directions. This includes the beams for the MOT and also the beams for the Rydberg excitation. The effective focal length is 33.1815 mm. All lenses in the objective have been coated for 405 nm, 770 nm and 1064 nm but the objective is only diffraction limited for 770 nm and 1064 nm. The resolution of the objective is sufficiently good to also address single atoms with the two-photon Rydberg excitation scheme.

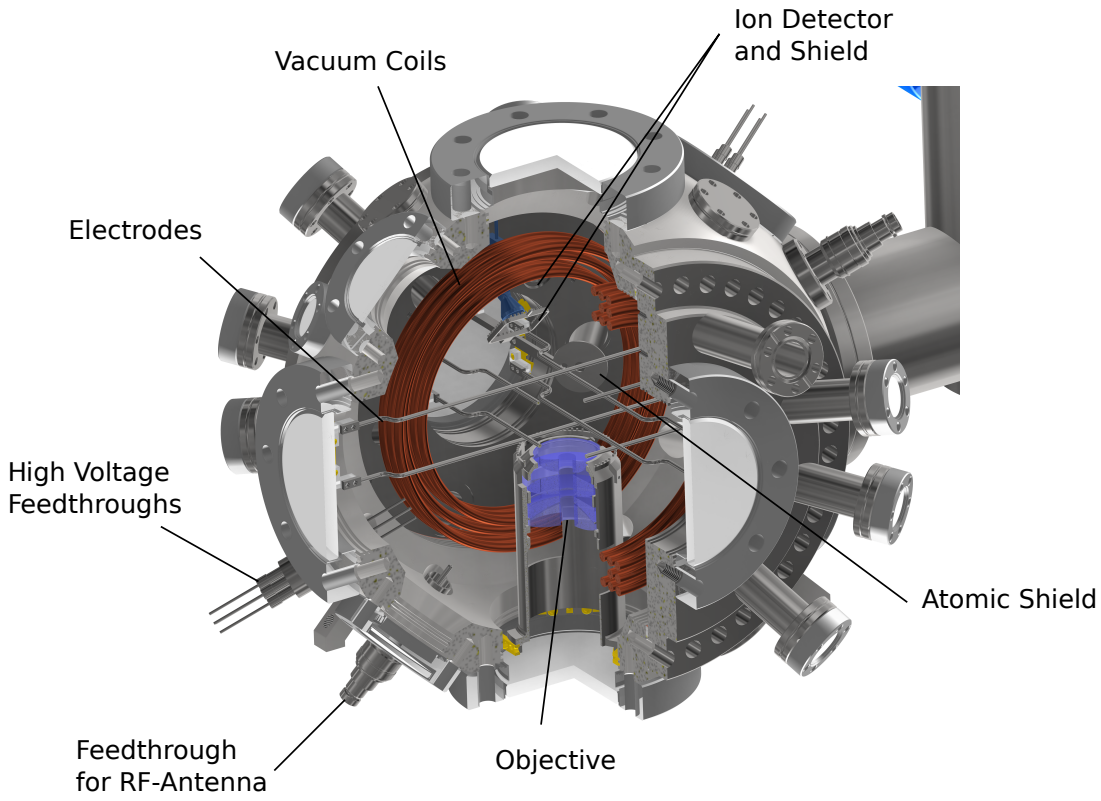

Figure 4.19 – Render of the vacuum chamber. This render shows a cross-sectional view of the vacuum chamber. Relevant components have been labeled and will be discussed in the context of the following paragraphs except for the atomic shield which blocks atoms that will not be captured in the magneto-optical trap.

Electrodes Control over the electric field is very important for Rydberg atoms. Especially for high principle quantum numbers n, the Rydberg atoms can be ionized by residual electric fields in the lab. The goal of the electrodes is to compensate these residual electric field (or generate electric fields) without inducing inhomogeneities. This means that we want to have the same electric field over the distance relevant for our experiment. To this end, we inserted eight electrodes into the vacuum system. The distances between the first parallel rods is chosen to be 32 mm in the horizontal and 27 mm in the vertical. The parallel rods have a horizontal distance of 28 mm and a vertical distance of 21 mm.

Ion Detector and Shield The channel electron multiplier in the setup (SJUTS KBL 10RS/45) helps us to detect ions from the ionization of the Rydberg atoms. This being said, it does not give us the same controllability as a quantum gas microscope does. Instead, it can help us for example to detect ionization of Rydberg atoms in a simple and quick fashion and for electric field ionization the detection is state selective. In front of the ion detector, we placed a ground shield made of golden wires to remove residual charges and reduce the number of dark counts on the ion detector.

Vacuum Coils The vacuum coils that e.g. create the magnetic field for the MOT are inside the vacuum chamber. The eight windings are in a configuration of three times three coils with one winding missing, in order to have some optical access through the coils. The coils can be water-cooled and are soldered to a hollow feedthrough. For the magneto-optical trap, the vacuum coils need to be able to provide a high magnetic field gradient. Our simulation shows that for a current of 200 A, we can achieve field gradients of about 40 G/cm in the axis of the coils and 20 G/cm in the perpendicular direction. Since we are not able to achieve a perfect Helmholtz configuration, especially important when we want a homogeneous field at the position of the atoms, we need to characterize the deviations. Figure 4.20b is a close up of 4.20a and shows the relative error from the field at the center of the coil configuration. One can see that the relative error will be below 10^{-3} at scales relevant for experiments.

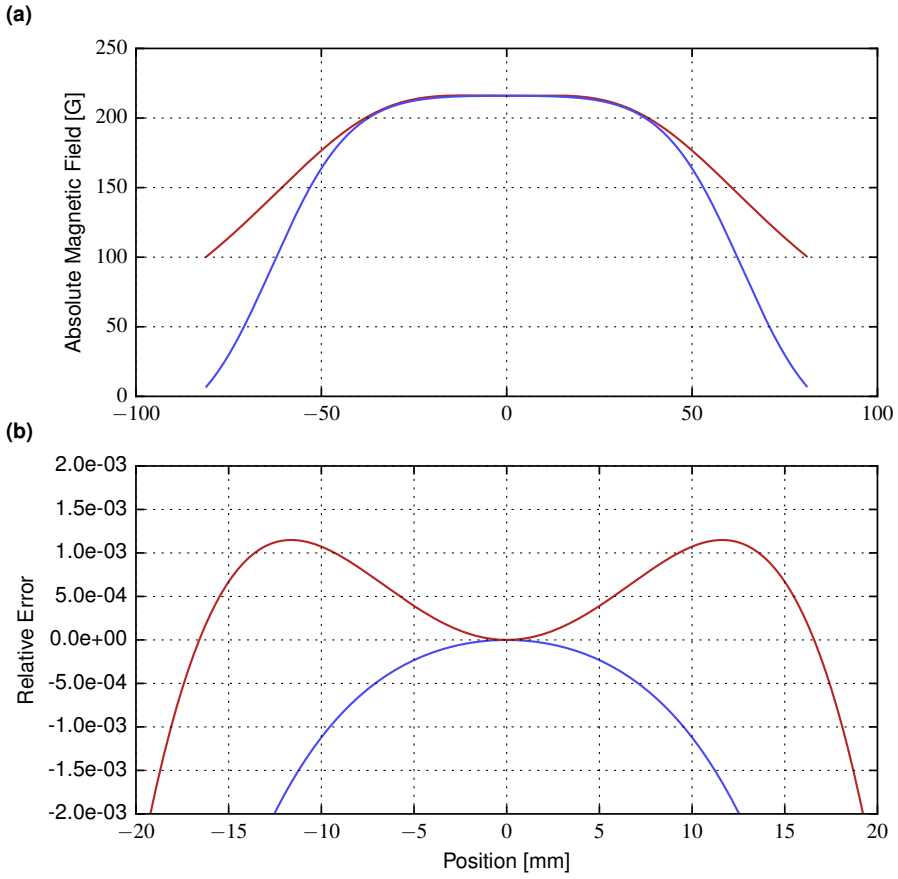

Figure 4.20 – Magnetic fields in Helmholtz configuration. a For a current of 200 A, we have plotted the absolute magnetic field at the center of the coil configuration. The red curve represents the magnetic field along the axis of the coils while the blue curve shows the magnetic field in the perpendicular direction. **b** A close-up of the upper figure. The plot range has been limited to capture the inhomogeneities expected in future experiments. The vertical axis has been rescaled to signify the relative error from the magnetic field at the center.

4.4 Zeeman Slower

4.4.1 Designing a Zeeman Slower for Potassium

A Zeeman slower and a 2D-MOT were considered for the pre-cooling stage of potassium. Despite the 2D-MOT being the common choice, we decided to build a Zeeman slower for multiple reasons. First, the laser setup only needs one additional beam that can be derived from the MOT-Laser with powers of about 10 mW. Furthermore, it allows to load Potassium-40 without using enriched potassium samples.

Inspired by the design in the Zwierlein group [97], we built a spin-flip Zeeman slower which has various advantages over a positive-field Zeeman slower. With a positive-field Zeeman slower and resonant lasers, the atoms will be pushed back into the Zeeman slower. In contrast, a spin-flip Zeeman slower can be operated for arbitrary long times. This allows us to stay flexible with the loading times. Additionally, we can achieve higher capture velocities with a lower magnetic fields. We undertook one special modification in comparison to the Zwierlein group. Instead of having a spin-flip Zeeman slower with two parts, the decreasing and the increasing part, we divided the increasing part into two different sections. One can see in Fig. 4.21 that the section that creates the opposite field is a block with three times three windings and an increasing part. We determined that adding another coil improves our results in the simulation and allows tuning the final velocity.

We can estimate the velocities that we can cool in the Zeeman slower given the temperature of the oven, the laser detuning and the magnetic fields that we can reach. Reasonable values are an oven temperature of 120 °C, a maximal magnetic field of 300 G at the beginning of the Zeeman slower and a laser detuning $\Delta_{Laser} = -2\pi \cdot 180\,MHz$. The detuning has been chosen such that other transitions or isotopes are not influenced by the laser. As the Zeeman slower only cools in the longitudonal direction, we will only be able to load atoms with low transversal velocities. From geometric considerations, we calculated the maximal transversal velocity, beginning from the nozzle of the oven, to be $v_{\perp,max} = 3\,m/s$. It should be noted that the loading rate and the average transversal velocity increase for higher temperature. The number density increases more (see graph for vapor pressure in [78]) than the average transversal velocity. Due to the low natural abundance, it will be useful to go to higher temperatures in the case of Potassium-40.

Before calculating the ideal field according to equation (3.16), we still need to determine the parameter μ' and the deceleration a. $\mu' = (g_{J'} m_{F'} - g_J m_F)\mu_B = \mu_B$ given that we transfer the atoms from the $m_F = 2$ to $m_{F'} = 3$ where $g_{J'} = 2/3$ while $g_J = 1/3$. The deceleration needs to be considered more carefully. While the maximal deceleration from (see equation (3.13)) is calculated to be $a_{max} = 252265\,m/s^2$, the so-called goodness factor needs to be estimated. It depends on two properties. First, the light force as a function of the intensity, given by equation (3.13). Since we cool on resonance, the saturation parameter is simply I/I_s. Second, it depends on the fraction

of the time that we are actually in the cooling transition. For circular polarized light one can treat the transitions as closed. With the possibility of linearly polarized light admixed, we can assume that the atoms will not remain within the desired transition at all times, especially not in the spin-flip region. Eventually, a deceleration of $a = 0.55 \cdot a_{max}$ was chosen to be realistic. Now that we have all the parameters for the ideal field, we can start simulating the windings.

4.4.2 Simulating the Windings

In the last subsection, we determined all necessary values to get a plot for the ideal field. Such a graph is represented by the red curve in Fig. 4.22a. Based on that computation, we simulate the coils that we distribute on the Zeeman slower.

In order to simulate the windings, we make use of a Python program. From the length of the Zeeman slower that we determined in the calculation of the ideal field, we needed to extract the lengths of the parts and the distance between them. Based on the lengths, the program calculates the number of windings that will fit in each layer. The coil configuration is determined by an array. The length of this array defines the number of layers on the Zeeman slower and the integer numbers within the array indicate the number of windings for each layer. At last, one defines the currents to simulate the magnetic field. Through an iterative process of changing the number of windings and currents, and similarly, the lengths of the different sections and the spacing between them, the simulation approaches the theoretical plot.

In Fig. 4.22a, the absolute value of the ideal field and the simulated field are plotted. The red curve represents the ideal field while the black curve shows the simulation. The difference between the simulation and the ideal field is substantial in the first part. The reason is that the windings start at the origin but not the slowing process of the atoms. Once the simulated field reaches 310 G, the simulation and the ideal field are in agreement up until a final velocity of the atoms which in this plot happens to be at $v_{\parallel,f} = 0\,m/s$. Figure 4.22b shows the absolute difference between the ideal field and the simulation. One can clearly see that once the simulation approaches the ideal field, the deviation remains below 4.3 G. To put this into terms of a frequency, the corresponding level shift of the hyperfine states is below one natural linewidth. In the figure, oscillations in the simulated field can be observed. These oscillations are caused by the discrete steps in the number of layers and therefore not avoidable. By changing the current settings, summarized in Table 4.10, it is possible to tune the final longitudinal velocity even close to $0\,m/s$. The special configuration for the Zeeman slower gives us the flexibility to choose the final velocity for the atoms leaving the Zeeman slower. These values are to be taken with care as they give a general idea of the current parameter regime and serve to show that we have tunability. With deviations from the ideal field below the natural linewidth and a tunable final velocity of the atoms, we can consider the simulation successful and turn to the physical realization of the Zeeman slower.

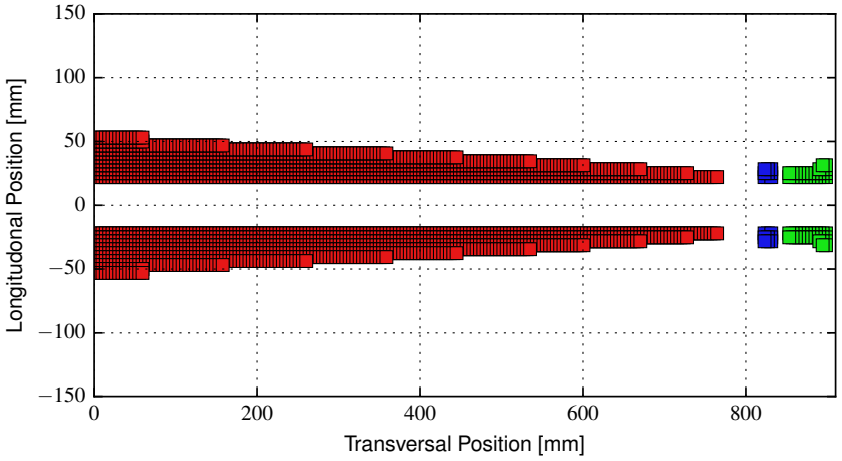

Figure 4.21 – Coil configuration of the Zeeman Slower. The coil configuration of the decreasing part is shown in red and the increasing part is shown in green. The block consisting of three times three windings is indicated in blue. The depicted configuration has been built and implemented in the setup.

Current [A]			
Decreasing	Block	Increasing	Final velocity $v_{\parallel,f}$ [m/s]
27	-9.5	-30	0
27	-9.5	-29	10
27	-9.5	-27	20
27	-9.8	-26.5	30
27	-9.8	-26	40

Table 4.10 – Zeeman slower currents and corresponding final velocities. The longitudinal final velocities of the atoms for different currents. The table stops at 40 m/s since the capture velocity of the atoms in the MOT will not exceed 40 m/s.

4.4.3 Winding the Zeeman slower

After determining the final configuration of the coils, we needed to wind the Zeeman slower. Given that the results in the simulation change noticeably by adding or removing one coil, it was important to recreate the simulation as accurately as possible. The hollow wires for the Zeeman slower were delivered by Luvata. The OF-OK® oxygen free copper wires have an outer dimension of 4x3 mm. The rectangular shape helps to wind the coils and reduces the twisting that the wires can experience. The inner diameter for water cooling is 2 mm. Finally, the wires are isolated by a kapton layer of 0.1 mm. The wire was wound over a non-magnetic stainless steel tube with a diameter of 4 cm. While each part respectively was electrically connected, the wires do not all share the same water connection. In general, each two layers share the same water connection for higher flow. In order to avoid shortcuts, each layer of coils was covered by kapton tape, glued (Polytec Duralco 128) and left to dry overnight.

After two weeks, we successfully finished the Zeeman slower and tested its mag-

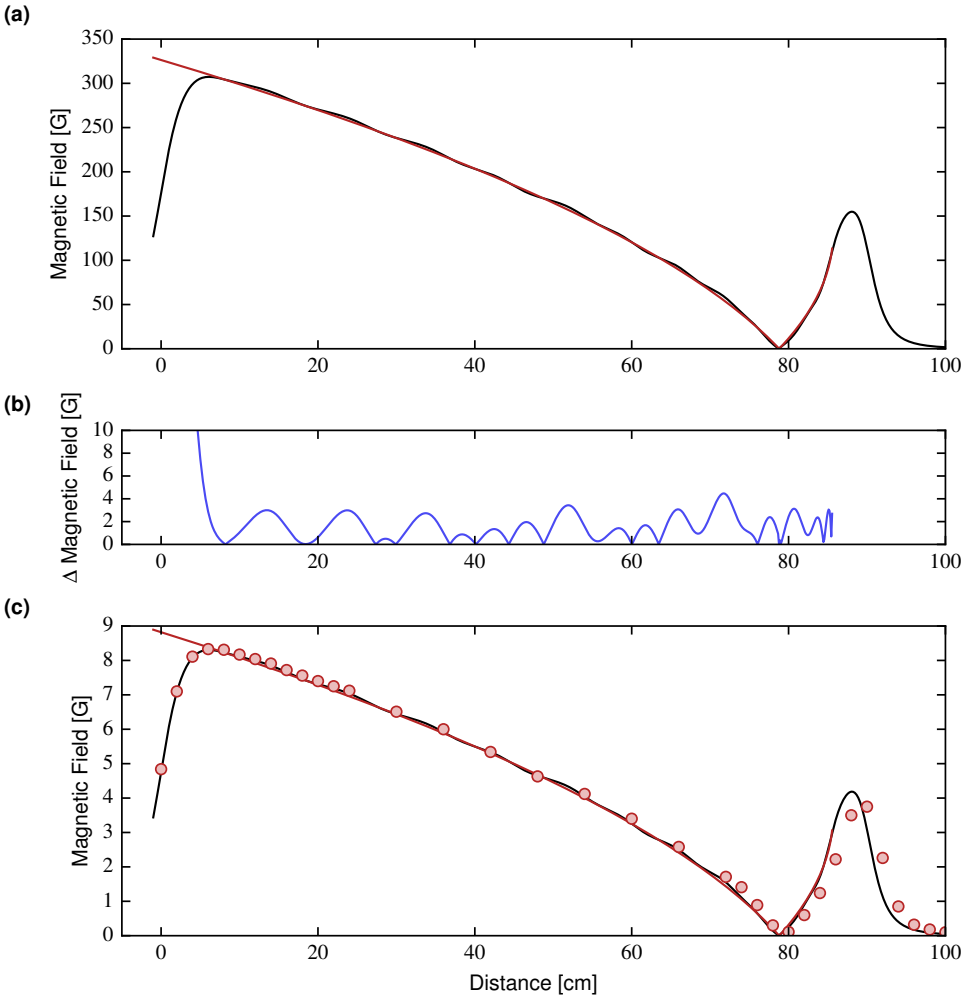

Figure 4.22 – Absolute value of the magnetic field in the Zeeman slower. **a** The ideal magnetic field is shown in red and the black curve corresponds to the simulated magnetic field. The final velocity for the ideal field is $v_{\parallel,f} = 0\,\mathrm{m/s}$. **b** The absolute value of the difference between the ideal magnetic field and the simulated one. This figure was used to optimize the coil configuration by minimizing the deviations. **c** A rescaled version of the simulated magnetic field and data points for the measurement.

netic field. The tests were intended not to reproduce the exact field but to see that there are no shorts in the Zeeman slower. The magnetic field probe can only measure on a scale of $-10\,\mathrm{G}$to $10\,\mathrm{G}$. Therefore we had to reduce the current without changing the current ratios between the different parts. The results can be seen in Fig. 4.22c. While the increasing part seems to fit the simulation, one can see a discrepancy in the increasing part. First of all, the field in the simulation is higher than in the measurement. This can be explained by the fact that we did not have a very precise current control. Second, the measurement exhibits a shift. The shift occurred during the winding of the Zeeman slower. It should have no effect on the performance of the Zeeman slower and just means that the atoms will be cooled for a short time off-resonantly before being cooled resonantly again. The low magnetic field region,

also called spin-flip region, allows the atoms to readjust to the magnetic field and to be pumped into the negative m_F-states. Consequently it is useful to have a spin-flip region for the Zeeman slower.

4.4.4 Zeeman Slower Repumper

Given that the transitions cannot be treated closed anymore, there is need for a repumper, also due to imperfections in the polarization. While losses during the spin-flip seem more prominent, one can understand that an atom being cooled undergoes thousands of cycles where leaving the desired cooling transitions once, will take the atom out of the cooling cycle.

In contrast to the repumper for the MOT and the grey molasses where we created different beams, the repumper is generated through an EOM. Before sending the beam for the Zeeman slower into the fiber, it passes through the EOM at a resonance frequency of 462 MHz, the ground state splitting. The power has been measured with a home-built photodiode to be $-15.5\,\mathrm{dB}$ compared to the carrier. Since the EOM contributes with this frequency to both directions from the carrier, the second sideband will cool the low velocity class. It will be left to see whether the sidebands will have any influence on the low velocity atoms.

4.4.5 Residual Fields

With magnetic fields of hundreds of Gauss within the Zeeman slower, the residual fields at the center of the vacuum chamber need to be considered. Residual fields can easily displace the center of the MOT and even worse, loading the magneto optical trap and suddenly switching off the Zeeman slower might instantaneously displace the MOT causing reheating and irreversible loss of the atoms. A look at Fig. 4.22 reveals that strong magnetic fields persist outside of the cooling range of the Zeeman slower. The distance from the last winding to the center of the vacuum chamber is approximately $14\,\mathrm{cm}$. For the realistic case that we want the longitudinal velocity of the atoms out of the Zeeman slower to be $v_{\parallel,f} = 30\,\mathrm{m/s}$, the residual field at the position of the MOT will be approximately 0.4 G. By ramping the current of the increasing part in the Zeeman slower, it is possible to reduce this offset. Going form $-29\,\mathrm{A}$ to $-10\,\mathrm{A}$ before switching of the current will lead to zero magnetic field at the center of the MOT cloud with magnetic fields below 0.02 G for the extension of the could, assuming a cloud radius of $5\,\mathrm{mm}$.

4.5 Magneto-Optical Trap and Grey Molasses

In this section, we are going to introduce the cooling sequence starting with a MOT on the D2 line, followed by a compressed MOT (CMOT) and the grey molasses on the D1 line. The main goal is to provide good starting parameters such as laser intensities and

detunings for the optimization of the cooling sequence. This being said, the cooling can be optimized for fast preparation times leading to fast experimental cycles or a high density for the preparation of a BEC. Thus, the cooling sequences will differ substantially. It is quite instructive to present these alternatives and their respective optimization strategies.

4.5.1 Beam Polarizations and Sizes

The polarization of the beams and their sizes do not change in the cooling sequence. Due to the recombination, beams going through the same fiber will have the same beam size and the polarization. We will use σ-polarized light for the Doppler and sub-Doppler cooling sequences. As motivated in 4.1, the transitions are the most closed when employing σ-polarized light.

The waists are chosen based on the velocity profile of the atoms leaving the Zeeman slower and on the physical constraint of the vacuum apparatus, especially the objective. Given a hole aperture of 8 mm for the objective, the beam diameter ($1/e^2$ of the peak intensity) in the vertical direction is chosen to be 8 mm. In the horizontal direction, we are estimating a beam diameter of 12 mm. The reason for this is the increased capture range, not to be confused with the capture velocity does not depend on the physical dimensions of the beams. The capture velocity indicates the velocity class that experiences a damping force while the capture range determines the atoms that can be trapped by the MOT. Having a larger beam will results in a deceleration over a larger distance and thus a bigger capture range. Note that there are two ways to increase the capture range. One is by sending in more power into the beam i.e. increasing the peak intensity and the other option is by increasing the waist. Two consideration led us to the choice of making the beam bigger. The obvious one is that we are limited in power. The less obvious is that inputting arbitrary large powers (see equation (3.13)) does not lead to an arbitrary big forces. Rather, the powers close the peak intensity is "unused". By increasing the beam, the peak intensity decreases and the deceleration distance for the atoms increases. On another note, the beam power imbalance, seen in Table 4.9, can be exploited by employing the least powerful beam on the vertical axis.

4.5.2 MOT

After the Zeeman slower the cooling scheme will begin with a MOT. In Table 4.11 we can see the preliminary detunings for the MOT and the grey molasses.

δ_{2C}	δ_{2R}	γ [G/cm]	I/I_{sat}	I_{2R}/I_{2C}
-3Γ	-3Γ	10	25	0.8

Table 4.11 – Initial parameters for the MOT. The table summarizes the detuning for the cooler and repumper on the 2D line, the magnetic field gradient and the intensities. The magnetic field gradient is given for the strong axis.

In Table 4.11 we can see the preliminary detunings for the MOT. From our discussion in 3.3, it is clear that the detuning needs to be red with respect to the transitions such that we get a force directed into the direction opposite to the velocity. The value of 3Γ represents a compromise between a higher capture velocity and more efficient cooling. From equation (3.18), we expect the lowest temperature for $\delta_{2C} = \Gamma/2$. On the other hand, this reduces our capture velocity by a factor six. One could implement a ramping sequence such that a higher capture velocity and lower temperatures can be achieved. With a tuning range of about 4Γ with our AOMs, one could start of with a larger detuning and reduce it while the atoms are cooling down. The values for the repumper and the magnetic field are in agreement with the values found in [71, 98].

Now we can also estimate the capture range of the MOT. It was already mentioned that the final longitudinal velocity $v_{\parallel,f}$ of the Zeeman slower and be tuned. In order for the atoms reach the MOT region, the final longitudinal velocity needs to be higher than $15\,\mathrm{m/s}$. The transversal velocity will be no higher than $3\,\mathrm{m/s}$. Thus, we only need to consider the longitudinal direction. The cooling force is given by equation (3.13) where we will assume that efficient cooling occurs only for $I/I_{sat} = 3$ and no cooling below. For a collimated Gaussian beam the intensity distribution is given by

$$I(z) = \frac{2P}{\pi w^2} \cdot e^{-2r^2/w^2}, \tag{4.3}$$

where the waist is $w = 6\,\mathrm{mm}$ and P is the total power. With a conservative guess that the power in one of the beams is $25\,\mathrm{mW}$, we will have an intensity of at least $3\,I_{sat}$ on a cooling distance of $12\,\mathrm{mm}$. Even though the cooling force does not only depend on the intensity but also on the detuning, we will assume that the atoms will be close to resonance as they are Doppler shifted into resonance due to their velocity i.e. $k \cdot v \sim \Delta = 3\Gamma$. After a small calculation of the deceleration and the time that the atoms are traveling through the laser, we can estimate the capture range to correspond to $30\,\mathrm{m/s}$.

At this point we should clarify how conservative our estimate is. The Zeeman slower has approximately an angle of 45° between the horizontal beams. Projecting the MOT beams onto the Zeeman slower axis leads to a higher capture range which we did not take into account. We ignored all cooling outside the $3\,I/I_{sat}$ region and the faster cooling rate close to the peak intensity. This calculation does not only give us insight about the capture range but also helps us to get intuition for the optimization of the parameters. It should also be understandable that the repumper should be at a similar detuning as the cooler in order for the repumper to also be resonant and for the atoms to remain in the cooling cycle. On another note, in order to fulfill the resonance condition the detuning of the cooler and the repumper should always scale with the final longitudinal velocity of the Zeeman slower $v_{\parallel,final}$.

4.5.3 Compressed MOT (CMOT)

After the MOT, that will be trapping the atoms and cool them down close to the Doppler temperature, the next step in the cooling sequence is a CMOT [99]. As mentioned in the beginning, the compressed MOT stage is optional and depends on the desired phase space density and the cycling time of the experiment. There are several ways to implement the compressed MOT. One of the possibilities is to increase the detuning, reduces the intensity and increase the magnetic field gradient. The magnetic field gradient will cause the cloud size to decrease. The combination of high detunings and low intensities leads to suppressed light-assisted collisions. This CMOT approach is implemented in [100].

Another possibility is to do a hybrid D1-D2 compressed MOT [71]. In such a case the temperatures that are reached in the compression are much lower. In such a case there is a D1 cooler and a D2 repumper. The authors indicate that a grey molasses cooling occur on the D1 line, the D2 light acts as a repumper and low magnetic fields of about 1 G/cm create a magnetic trapping. As the grey molasses is very sensitive to magnetic fields, low magnetic field gradients were chosen.

4.5.4 Grey Molasses

The last optical cooling step is the grey molasses scheme on the D1 line. The temperatures that we can expect are around 10 µK. Table 4.12 summarizes the values that can be used as a starting point to perform the grey molasses depending on the previous cooling step.

Preceding step in sequence	δ_{1C}	δ_{1R}	I_{1C}/I_{sat}	I_{1R}/I_{1C}
MOT	5Γ	5Γ	3	1
D2 compressed MOT	5Γ	5Γ	15	1
D1-D2 compressed MOT	5Γ	5Γ	4	1

Table 4.12 – Initial parameters for grey molasses cooling. The detunings and intensities for the grey molasses are summarized according to the preceding cooling step.

We can see that the blue detuning of the lasers and the Raman condition are fulfilled and therefore the conditions that we based the grey molasses discussion on in section 3.4. It is still left to answer with which magnitude we detune the lasers. While the detunings for the MOT can be estimated from intuitive arguments, this is not possible for the grey molasses. Thus, inspired by the literature [71, 80], $\delta_{1C} = \delta_{1R} = 5\Gamma$ will be a good starting point for the experiment.

The intensity parameters on the other hand can be estimated. It turns out to be useful to perform the grey molasses in two steps. The first part of the sequence optimizes the capture velocity while the second one optimizes the temperature. In order to optimize the capture velocity for the grey molasses, we want to fulfill the condition

given in equation (3.24). As Γ_{eff} is proportional to intensity, we want to use high intensities. While given in the table as $10\, I/I_{sat}$, it clearly depends on the temperatures that the atoms will have after the compressed MOT. For the next part in the sequence, the detunings remain the same but the intensity is ramped down. In equation (3.23) we have also seen that the temperature limit also scales with the intensity. It follows that ramping down the intensity of the laser will reduce the temperature. As a reminder, this argument breaks down once we are getting close to the recoil limit. In [71] the high-intensity sequence is applied for about $2\,ms$ and the ramp to almost zero intensity takes about $7\,ms$. In this example it should be noted the grey molasses followed the D1-D2 compressed MOT where the CMOT temperatures are low compared to the D2 compressed MOT.

CHAPTER 5

Conclusion and Outlook

5.1 Conclusion

In this thesis, we have examined the progress for the construction of a new experimental platform for quantum simulation with Rydberg atoms. In particular, we have presented and characterized the laser system for cooling and trapping of Potassium-39. Additionally, have discussed the general vacuum system and the vacuum chamber.

In the beginning of this thesis, we derived the light forces for atoms in the presence of light and explained the working principle for the magneto-optical trap and the grey molasses. Followed by a summary of the properties of potassium, we phrased the requirements on the laser system for the trapping and cooling of Potassium-39. In the subsequent sections, we discussed the laser system starting from the general idea to the concrete realization. We presented the lasers that were employed in the setup, explained the FM error signal generation and how to lock the lasers. We then measured the power amplification of the tapered amplifiers, the bandwidth of the acousto-optical modulators to shift the laser frequency and the fiber coupling efficiencies. The characterization of the laser system and the Zeeman slower showed us that the requirements for Doppler and sub-Doppler cooling were fulfilled. In particular, we showed that sufficient powers are available for the cooler and repumper beams and that the frequencies can be tuned and locked with lineshapes far below the natural linewidth. With the simulation and construction of the Zeeman slower, we were able to finally propose concrete laser parameters for the various cooling stages. Furthermore, the strategies to optimize these parameters were discussed.

This thesis reported on the vacuum system that combines ultra-high vacuum and high flux of potassium. In particular, we presented the vacuum chamber. Sufficient magnetic field gradients in combination with optical access due to the multitude of viewports allow the realization of Doppler and sub-Doppler cooling. Furthermore, we presented the components inside the vacuum chamber and their role for a quantum simulator with Rydberg atoms.

5.2 Outlook

The completion of the vacuum assembly and the laser system will soon allow for the first observation of atoms inside the magneto-optical trap. With the optimization of the cooling sequences, it will be interesting to see what kind cycle times can be achieved with the experimental apparatus.

After the optimization of the MOT, the first tests for loading microtraps and unity-filling inside the microtraps can be performed. To this end, the laser system in the D1 line needs to be redesigned. The laser for the blue shielding and the cooling in the microtraps need to be offset-locked to have tunabilities of several hundreds of mega-hertz. A master-slave setup will be suitable where one of the D1 lasers is locked to a spectroscopy while the other lasers will be locked with respect to that laser. During the redesign and construction it will be possible to determine whether the Doppler temperature is sufficiently low for the loading of the microtraps or whether sub-Doppler cooling is needed.

In parallel, the construction of two laser systems for the excitation of Rydberg atoms will be built. For the two-photon excitation, it will be interesting to explore other spectroscopies aside from FM spectroscopy. This will be relevant for the reduction of laser-induced decoherences in the Rydberg excitation. A more elaborate measurement of the laser linewidth and an optimization of the lock can be explored. Additionally, the construction of the UV laser system for single-photon excitation has started. It will be fascinating to see the efficiencies for the generation of UV light and to perform Rydberg spectroscopy.

Bibliography

1. Metcalf, H. J. & van der Straten, P. *Laser Cooling and Trapping* (Springer New York, New York, NY, 1999) (cit. on p. 1).
2. Ashkin, A. Trapping of Atoms by Resonance Radiation Pressure. *Physical Review Letters* **40,** 729–732 (1978) (cit. on p. 1).
3. Hänsch, T. & Schawlow, A. Cooling of gases by laser radiation. *Optics Communications* **13,** 68–69 (1975) (cit. on p. 1).
4. Andreev, S. V., Balykin, V. I., Letokhov, V. & Minogin, V. Radiative slowing and reduction of the energy spread of a beam of sodium to 1.5K in an opposite directed laser beam. *JETP Lett.* **34,** 442–445 (1981) (cit. on p. 1).
5. Prodan, J. V. & Phillips, W. D. Chirping the light—fantastic? Recent NBS atom cooling experiments. *Progress in Quantum Electronics* **8,** 231–235 (1984) (cit. on pp. 1, 10).
6. Ertmer, W, Blatt, R, Hall, J. L. & Zhu, M. Laser Manipulation of Atomic Beam Velocities: Demonstration of Stopped Atoms and Velocity Reversal. *Physical Review Letters* **54,** 996–999 (1985) (cit. on p. 1).
7. Chu, S., Hollberg, L, Bjorkholm, J. E., Cable, A. & Ashkin, A. Three-dimensional viscous confinement and cooling of atoms by resonance radiation pressure. *Physical Review Letters* **55,** 48–51 (1985) (cit. on p. 1).
8. Raab, E. L., Prentiss, M., Cable, A., Chu, S. & Pritchard, D. E. Trapping of Neutral Sodium Atoms with Radiation Pressure. *Physical Review Letters* **59,** 2631–2634 (1987) (cit. on pp. 1, 11).
9. Aspect, A, Arimondo, E, Kaiser, R, Vansteenkiste, N & Cohen-Tannoudji, C. Laser Cooling below the One-Photon Recoil Energy by Velocity-Selective Coherent Population Trapping. *Physical Review Letters* **61,** 826–829 (1988) (cit. on p. 1).
10. Anderson, M. H., Ensher, J. R., Matthews, M. R., Wieman, C. E. & Cornell, E. A. Observation of Bose-Einstein Condensation in a Dilute Atomic Vapor. *Science* **269,** 198–201 (1995) (cit. on p. 1).
11. Davis, K. B. *et al.* Bose-Einstein Condensation in a Gas of Sodium Atoms. *Physical Review Letters* **75,** 3969–3973 (1995) (cit. on p. 1).
12. Andrews, M. R. Observation of Interference Between Two Bose Condensates. *Science* **275,** 637–641 (1997) (cit. on p. 1).
13. Bloch, I., Hänsch, T. W. & Esslinger, T. Atom Laser with a cw Output Coupler. *Physical Review Letters* **82,** 3008–3011 (1999) (cit. on p. 1).

14. Jaksch, D, Bruder, C, Cirac, J. I., Gardiner, C. W. & Zoller, P. Cold Bosonic Atoms in Optical Lattices. *Physical Review Letters* **81,** 3108–3111 (1998) (cit. on p. 1).

15. Hubbard, J. Electron Correlations in Narrow Energy Bands. *Proceedings of the Royal Society A: Mathematical, Physical and Engineering Sciences* **276,** 238–257 (1963) (cit. on p. 1).

16. Greiner, M., Mandel, O., Esslinger, T., Hänsch, T. W. & Bloch, I. Quantum phase transition from a superfluid to a Mott insulator in a gas of ultracold atoms. *Nature* **415,** 39–44 (2002) (cit. on pp. 1, 4).

17. Bakr, W. S., Gillen, J. I., Peng, A., Fölling, S. & Greiner, M. A quantum gas microscope for detecting single atoms in a Hubbard-regime optical lattice. *Nature* **462,** 74–77 (2009) (cit. on pp. 1, 4).

18. Trotzky, S *et al.* Time-Resolved Observation and Control of Superexchange Interactions with Ultracold Atoms in Optical Lattices. *Science* **319,** 295–299 (2008) (cit. on p. 1).

19. Baier, S *et al.* Extended Bose-Hubbard models with ultracold magnetic atoms. *Science* **352,** 201–205 (2016) (cit. on p. 1).

20. Aikawa, K *et al.* Bose-Einstein Condensation of Erbium. *Physical Review Letters* **108,** 210401 (2012) (cit. on p. 1).

21. Lu, M., Burdick, N. Q., Youn, S. H. & Lev, B. L. Strongly Dipolar Bose-Einstein Condensate of Dysprosium. *Physical Review Letters* **107,** 190401 (2011) (cit. on p. 1).

22. Griesmaier, A., Werner, J., Hensler, S., Stuhler, J. & Pfau, T. Bose-Einstein Condensation of Chromium. *Physical Review Letters* **94,** 160401 (2005) (cit. on p. 1).

23. Hazzard, K. R. A. *et al.* Many-Body Dynamics of Dipolar Molecules in an Optical Lattice. *Physical Review Letters* **113,** 195302 (2014) (cit. on p. 1).

24. Löw, R. *et al.* An experimental and theoretical guide to strongly interacting Rydberg gases. *Journal of Physics B: Atomic, Molecular and Optical Physics* **45,** 113001 (2012) (cit. on pp. 1, 3).

25. Cinti, F *et al.* Supersolid Droplet Crystal in a Dipole-Blockaded Gas. *Physical Review Letters* **105,** 135301 (2010) (cit. on p. 1).

26. Dalla Torre, E. G., Berg, E. & Altman, E. Hidden Order in 1D Bose Insulators. *Physical Review Letters* **97,** 260401 (2006) (cit. on p. 1).

27. Mattioli, M., Dalmonte, M., Lechner, W. & Pupillo, G. Cluster Luttinger Liquids of Rydberg-Dressed Atoms in Optical Lattices. *Physical Review Letters* **111,** 165302 (2013) (cit. on p. 1).

28. Schauss, P. *et al.* Crystallization in Ising quantum magnets. *Science* **347,** 1455–1458 (2015) (cit. on pp. 1, 5).

29. Zeiher, J. *et al.* Many-body interferometry of a Rydberg-dressed spin lattice. *Nature Physics* **12,** 1095–1099 (2016) (cit. on p. 1).

30. Bloch, I., Dalibard, J. & Zwerger, W. Many-body physics with ultracold gases. *Reviews of Modern Physics* **80,** 885–964 (2008) (cit. on p. 3).
31. Georgescu, I. M., Ashhab, S & Nori, F. Quantum simulation. *Reviews of Modern Physics* **86,** 153–185 (2014) (cit. on p. 3).
32. Khemani, V., Lazarides, A., Moessner, R. & Sondhi, S. L. Phase Structure of Driven Quantum Systems. *Physical Review Letters* **116,** 250401 (2016) (cit. on pp. 3, 5).
33. Polkovnikov, A., Sengupta, K., Silva, A. & Vengalattore, M. Colloquium : Nonequilibrium dynamics of closed interacting quantum systems. *Reviews of Modern Physics* **83,** 863–883 (2011) (cit. on p. 3).
34. Saffman, M, Walker, T. G. & Mølmer, K. Quantum information with Rydberg atoms. *Reviews of Modern Physics* **82,** 2313–2363 (2010) (cit. on p. 3).
35. Jaksch, D *et al.* Fast Quantum Gates for Neutral Atoms. *Physical Review Letters* **85,** 2208–2211 (2000) (cit. on p. 3).
36. Anderson, W. R., Veale, J. R. & Gallagher, T. F. Resonant Dipole-Dipole Energy Transfer in a Nearly Frozen Rydberg Gas. *Physical Review Letters* **80,** 249–252 (1998) (cit. on p. 3).
37. Mack, M. *et al.* All-optical measurement of Rydberg-state lifetimes. *Physical Review A* **92,** 012517 (2015) (cit. on p. 3).
38. Balewski, J. B. *et al.* Rydberg dressing: understanding of collective many-body effects and implications for experiments. *New Journal of Physics* **16,** 063012 (2014) (cit. on p. 3).
39. Johnson, J. E. & Rolston, S. L. Interactions between Rydberg-dressed atoms. *Physical Review A* **82,** 033412 (2010) (cit. on p. 3).
40. Honer, J., Weimer, H., Pfau, T. & Büchler, H. P. Collective Many-Body Interaction in Rydberg Dressed Atoms. *Physical Review Letters* **105,** 160404 (2010) (cit. on p. 3).
41. Müller, M, Lesanovsky, I, Weimer, H, Büchler, H. P. & Zoller, P. Mesoscopic Rydberg Gate Based on Electromagnetically Induced Transparency. *Physical Review Letters* **102,** 170502 (2009) (cit. on p. 3).
42. Schauß, P. *et al.* Observation of mesoscopic crystalline structures in a two-dimensional Rydberg gas (2012) (cit. on p. 4).
43. Zeiher, J. *Realization of Rydberg-dressed quantum magnets* PhD thesis (Ludwig-Maxmillians-Universität München, 2017) (cit. on pp. 4, 38).
44. Sherson, J. F. *et al.* Single-atom-resolved fluorescence imaging of an atomic Mott insulator. *Nature* **467,** 68–72 (2010) (cit. on p. 4).
45. Cheuk, L. W. *et al.* Quantum-Gas Microscope for Fermionic Atoms. *Physical Review Letters* **114,** 193001 (2015) (cit. on p. 4).
46. Hilker, T. A. *et al.* Revealing hidden antiferromagnetic correlations in doped Hubbard chains via string correlators. *Science* **357,** 484–487 (2017) (cit. on p. 4).

47. Bloch, I. Ultracold quantum gases in optical lattices. *Nature Physics* **1,** 23–30 (2005) (cit. on p. 4).

48. Abanin, D. A. & Demler, E. Measuring Entanglement Entropy of a Generic Many-Body System with a Quantum Switch. *Physical Review Letters* **109,** 020504 (2012) (cit. on p. 5).

49. Henkel, N, Nath, R & Pohl, T. Three-Dimensional Roton Excitations and Supersolid Formation in Rydberg-Excited Bose-Einstein Condensates. *Physical Review Letters* **104,** 195302 (2010) (cit. on p. 5).

50. Pupillo, G, Micheli, A, Boninsegni, M, Lesanovsky, I & Zoller, P. Strongly Correlated Gases of Rydberg-Dressed Atoms: Quantum and Classical Dynamics. *Physical Review Letters* **104,** 223002 (2010) (cit. on p. 5).

51. Yao, N. Y., Potter, A. C., Potirniche, I.-D & Vishwanath, A. Discrete Time Crystals: Rigidity, Criticality, and Realizations. *Physical Review Letters* **118,** 030401 (2017) (cit. on p. 5).

52. Isenhower, L *et al.* Demonstration of a Neutral Atom Controlled-NOT Quantum Gate. *Physical Review Letters* **104,** 010503 (2010) (cit. on p. 5).

53. Glaetzle, A. W. *et al.* Quantum Spin-Ice and Dimer Models with Rydberg Atoms. *Physical Review X* **4,** 041037 (2014) (cit. on p. 5).

54. Glaetzle, A. W. *et al.* Designing Frustrated Quantum Magnets with Laser-Dressed Rydberg Atoms. *Physical Review Letters* **114,** 173002 (2015) (cit. on p. 5).

55. Gordon, J. P. & Ashkin, A. Motion of atoms in a radiation trap. *Physical Review A* **21,** 1606–1617 (1980) (cit. on p. 7).

56. Gardiner, C. & Zoller, P. *Quantum Noise* 3rd, 450 (Springer Berlin (Verlag), Berlin, Heidelberg, 2004) (cit. on p. 7).

57. Cohen-Tannoudji, C., Dupont-Roc, J. & Grynberg, G. *Atom-Photon Interactions* (Wiley-VCH Verlag GmbH, Weinheim, Germany, 1998) (cit. on p. 8).

58. Cohen-Tannoudji, C. *Atomic Motion in Laser Light* (eds Dalibard, J., Raimond, J. & Zinn Justin, J.) 1–164 (Elsevier Science Publisher B.V., 1992) (cit. on p. 8).

59. Steck, D. A. *Quantum Optics* (eds Walls, D. & Milburn, G. J.) 932. arXiv: `arXiv:1011.1669v3` (Springer Berlin Heidelberg, Berlin, Heidelberg, 2008) (cit. on p. 9).

60. Chu, S., Bjorkholm, J. E., Ashkin, A. & Cable, A. Experimental Observation of Optically Trapped Atoms. *Physical Review Letters* **57,** 314–317 (1986) (cit. on p. 9).

61. Grimm, R., Weidemüller, M. & Ovchinnikov, Y. B. in *Adv. At. Mol. Opt. Phys.* 95–170 (2000). arXiv: `9902072 [physics]` (cit. on p. 9).

62. Zirbel, J. J. *et al.* Heteronuclear molecules in an optical dipole trap. *Physical Review A* **78,** 013416 (2008) (cit. on p. 9).

63. Ashkin, A., Dziedzic, J. M., Bjorkholm, J. E. & Chu, S. Observation of a single-beam gradient force optical trap for dielectric particles. *Optics Letters* **11,** 288 (1986) (cit. on p. 9).

64. Nogrette, F *et al.* Single-Atom Trapping in Holographic 2D Arrays of Microtraps with Arbitrary Geometries. *Physical Review X* **4,** 021034 (2014) (cit. on p. 9).
65. Ashkin, A. & Gordon, J. P. Stability of radiation-pressure particle traps: an optical Earnshaw theorem. *Optics Letters* **8,** 511 (1983) (cit. on p. 11).
66. Lett, P. D. *et al.* Optical molasses. *Journal of the Optical Society of America B* **6,** 2084 (1989) (cit. on p. 12).
67. Metcalf, H. J. & van der Straten, P. *Laser Cooling and Trapping* 328 (Springer New York, New York, NY, 1999) (cit. on pp. 13, 20).
68. Dalibard, J. & Cohen-Tannoudji, C. Laser cooling below the Doppler limit by polarization gradients: simple theoretical models. *Journal of the Optical Society of America B* **6,** 2023 (1989) (cit. on pp. 13, 14).
69. Boiron, D., Triché, C., Meacher, D. R., Verkerk, P. & Grynberg, G. Three-dimensional cooling of cesium atoms in four-beam gray optical molasses. *Physical Review A* **52,** R3425–R3428 (1995) (cit. on pp. 13, 15).
70. Ungar, P. J., Weiss, D. S., Riis, E. & Chu, S. Optical molasses and multilevel atoms: theory. *Journal of the Optical Society of America B* **6,** 2058 (1989) (cit. on p. 13).
71. Salomon, G *et al.* Gray-molasses cooling of 39 K to a high phase-space density. *EPL (Europhysics Letters)* **104,** 63002 (2013) (cit. on pp. 15, 21, 62–64).
72. Landini, M *et al.* Sub-Doppler laser cooling of potassium atoms. *Physical Review A* **84** (2011) (cit. on p. 15).
73. Bambini, A. & Agresti, A. Radiative cooling force in atoms with multiplet structure. *Physical Review A* **56,** 3040–3055 (1997) (cit. on p. 15).
74. Esslinger, T. *et al.* Purely optical dark lattice. *Optics Letters* **21,** 991 (1996) (cit. on p. 15).
75. Papoff, F., Mauri, F. & Arimondo, E. Transient velocity-selective coherent population trapping in one dimension. *Journal of the Optical Society of America B* **9,** 321 (1992) (cit. on p. 16).
76. Tarnowski, M. *Implementation and Characterization of a Gray Molasses and of Tunable Hexagonal Optical Lattices for 40 K* PhD thesis (Universität Hamburg, 2015) (cit. on p. 17).
77. Grünzweig, T, Hilliard, A, McGovern, M. & Andersen, M. F. Near-deterministic preparation of a single atom in an optical microtrap. *Nature Physics* **6,** 951–954 (2010) (cit. on p. 19).
78. Tiecke, T. G. *Feshbach resonances in ultracold mixtures of the fermionic quantum gases 6Li and 40K* PhD thesis (University of Amsterdam, 2009) (cit. on pp. 20, 56).
79. Cohen-Tannoudji, C., Diu, B. & Laloe, F. *Quantum Mechanics, Volume 1* (Wiley-VCH Verlag GmbH, 1977) (cit. on p. 20).
80. Rio Fernandes, D. *et al.* Sub-Doppler laser cooling of fermionic 40 K atoms in three-dimensional gray optical molasses. *EPL (Europhysics Letters)* **100,** 63001 (2012) (cit. on pp. 22, 63).

81. Baillard, X *et al.* Interference-filter-stabilized external-cavity diode lasers. *Optics Communications* **266,** 609–613 (2006) (cit. on p. 26).
82. Svelto, O. *Principles of Lasers* 49 (Springer US, Boston, MA, 2010) (cit. on p. 27).
83. Mercer, L. 1/f frequency noise effects on self-heterodyne linewidth measurements. *Journal of Lightwave Technology* **9,** 485–493 (1991) (cit. on p. 28).
84. Elliott, D. S., Roy, R. & Smith, S. J. Extracavity laser band-shape and bandwidth modification. *Physical Review A* **26,** 12–18 (1982) (cit. on p. 28).
85. Di Domenico, G., Schilt, S. & Thomann, P. Simple approach to the relation between laser frequency noise and laser line shape. *Applied Optics* **49,** 4801 (2010) (cit. on p. 28).
86. Ricci, L. *et al.* A compact grating-stabilized diode laser system for atomic physics. *Optics Communications* **117,** 541–549 (1995) (cit. on p. 29).
87. Cook, E. C., Martin, P. J., Brown-Heft, T. L., Garman, J. C. & Steck, D. A. High passive-stability diode-laser design for use in atomic-physics experiments. *Review of Scientific Instruments* **83,** 043101 (2012) (cit. on p. 29).
88. Preston, D. W. Dopplerfree saturated absorption: Laser spectroscopy. *American Journal of Physics* **64,** 1432–1436 (1996) (cit. on p. 32).
89. Demtröder, W. *Laserspektroskopie 1* 49 (Springer Berlin Heidelberg, Berlin, Heidelberg, 2011) (cit. on p. 32).
90. Bjorklund, G. C. Frequency-modulation spectroscopy: a new method for measuring weak absorptions and dispersions. *Optics Letters* **5,** 15 (1980) (cit. on pp. 33, 34).
91. Supplee, J. M., Whittaker, E. a. & Lenth, W. Theoretical description of frequency modulation and wavelength modulation spectroscopy. *Applied Optics* **33,** 6294 (1994) (cit. on p. 34).
92. Purves, G. T. *Absorption and Dispersion In Atomic Vapours: Applications To Interferometery* PhD thesis (Durham University, 2006) (cit. on p. 35).
93. *Springer Handbook of Lasers and Optics* (ed Träger, F.) **8,** 085201 (Springer Berlin Heidelberg, Berlin, Heidelberg, 2012) (cit. on p. 39).
94. Donley, E. A., Heavner, T. P., Levi, F., Tataw, M. O. & Jefferts, S. R. Double-pass acousto-optic modulator system. *Review of Scientific Instruments* **76,** 063112 (2005) (cit. on p. 47).
95. O'Hanlon, J. *A User's Guide to Vacuum Technology A User's Guide to Vacuum Technology Third Edition* 3rd, 536 (Wiley, 2003) (cit. on p. 52).
96. Hoffman, D. M., Thomas, J. H. & Singh, B. *Handbook of Vacuum Science and Technology* 835 (Elsevier Science, 1997) (cit. on p. 52).
97. Wu, C.-H. *Strongly Interacting Quantum Mixtures of Ultracold Atoms* PhD thesis (Massachusetts Institute of Technology, 2013) (cit. on p. 56).
98. Landini, M. *A tunable Bose-Einstein condensate for quantum interferometry* PhD thesis (University of Trento, 2008) (cit. on p. 62).

99. Petrich, W., Anderson, M. H., Ensher, J. R. & Cornell, E. A. Behavior of atoms in a compressed magneto-optical trap. *Journal of the Optical Society of America B* **11,** 1332 (1994) (cit. on p. 63).

100. Landini, M *et al.* Direct evaporative cooling of 39 K atoms to Bose-Einstein condensation. *Physical Review A* **86,** 033421 (2012) (cit. on p. 63).

List of Figures

List of Tables

Acknowledgement

This thesis was a great experience for me. It was wonderful to not only learn something from a textbook where things can feel quite distant but to apply it and to see results, well, and sometimes not to see results. In the atmosphere of the Bloch group, it felt like struggling was not suffering and problems were merely hurdles. At times it was also very competitive, ... after lunch around the table soccer. Thank you for creating such a great atmosphere to work and enjoy work.

At this point, I would like to thank the people around me that have helped me. First, a special thanks to Anton, Olivia and Karsten. It was a wonderful feeling to know that I could to come them with problems and that they helped me goodheartedly in all possible ways. Needless to say how important they were for the progress in building the experiment. Thanks to Kristina. Not only was Kristina essential for the organizational aspects in the Bloch group but she especially took great interest in our well-being. Next, I would like to thank Immanuel. Once, for having suggested to me to contact Christian for a Master's thesis but also for the talk he gave during my Bachelor's time at the Technion which was one of the reasons for me to pursue my Master's studies in Munich. I would like to thank Guillaume for the time he took to answer my questions patiently, especially on the topic of grey molasses and Simon who was always ready for physics discussions. I want to express my very great appreciation to Christian who is great supervisor. I believe that Christian wants the best for us and the best in us. Again, thanks for answering all the questions I had (and there were many), proofreading my thesis, advising me on the internship in Florence etc. With this, I would like thank Lorenzo and Nikolaus for the help they provided me during this thesis. It was a great time to work with them. I think that they have taught me to work in a more proper fashion and yet, they have accepted by "N-1"-rule on screws. I need to especially thank them for reading and editing my thesis without giving up on me. Last but not least, a special thanks goes to Denise and my cat Griffin. They have accompanied me through this time of writing the thesis and endured me when I was being difficult. Denise knew that coming back to Germany would be difficult for me but she provided a loving home.

Erklärung

Hiermit erkläre ich, die vorliegende Arbeit selbständig verfasst zu haben und keine anderen als die in der Arbeit angegebenen Quellen und Hilfsmittel benutzt zu haben.

Ort, Datum

Unterschrift